

# Smooth surface reconstruction of earthquake faults from distributed potency beachballs

Dye SK Sato<sup>1</sup>, Yuji Yagi<sup>2</sup>, Ryo Okuwaki<sup>2</sup>, & Yukitoshi Fukahata<sup>3</sup>

<sup>1</sup> *Research Institute for Marine Geodynamics, Japan Agency for Marine-Earth Science and Technology, Yokohama, Kanagawa 236-0001, Japan*

<sup>2</sup> *Institute of Life and Environmental Sciences, University of Tsukuba, Tsukuba, Ibaraki 305-8572, Japan*

<sup>3</sup> *Disaster Prevention Research Institute, Kyoto University, Uji, Kyoto 611-0011, Japan*

## SUMMARY

Earthquake faults approximate smooth surfaces of displacement discontinuity in a coarse-grained linear continuum, and the beachball nodal planes of source inelastic strain (potency) indicate the normal vector ( $n$ -vector) of the crack face. This theoretical relation has been used to interpret estimated potency as geometrical information of earthquake faults. We formulate an inverse analysis for reconstructing a smooth, three-dimensional fault surface from a given potency field. The analysis is grounded on the definition of the  $n$ -vector that is orthogonality to a surface. It is shown from this definition that, whereas the estimated  $n$ -vector field is always explained by a unique curve in two dimensions, the surface reconstruction from the estimated  $n$ -vector field is an overdetermined problem with no solution in three dimensions. We resolve this overdetermination by adopting the original definition of a fault surface as a map that approximates a thin sheet of potency onto a displacement discontinuity across a literal face. An analytical expression for this fault reconstruction is derived and confirmed to reproduce the original three-dimensional smooth surface from a synthesized noisy  $n$ -vector field. By incorporating this result into surface reconstruction based on potency density tensor inversion, we estimate the three-

dimensional source fault geometry of the 2013 Balochistan earthquake. The estimated geometry is more consistent with the fault trace than the quasi-two-dimensional shape reconstruction as anticipated by our numerical experiments.

**Key words:** Earthquake source observations; Fractures, faults, and high strain deformation zones; Inverse theory; Theoretical seismology

## 1 INTRODUCTION

Fault geometry predestines potential rupture modes and arrests of earthquakes (Das & Aki 1977; Aki 1979; Kase & Day 2006; Bruhat et al. 2016; Ozawa et al. 2023). Therefore, fault geometry inference from actual data serves as a grasp of the source complexity that happened (Barka & Kadinsky-Cade 1988; Kodaira et al. 2006; Ando & Kaneko 2018; Howarth et al. 2021).

Great efforts accumulate to extract information on source fault geometry from observed data (e.g., Matsu'ura & Hasegawa 1987; Volkov et al. 2017; Dutta et al. 2021). The simplest, highly successful example is a configuration estimation using a point or rectangular fault, which infers the center of masses, angles, and lengths of a fault (Matsu'ura & Hasegawa 1987). Detailed slip patterns could be estimated from a distributed slip inversion on a prescribed fault surface (Yabuki & Matsu'ura 1992).

Still, the inference of fault non-planarity is challenging. Fault subdivisions with planar subfaults have been heavily utilized in practice (e.g., Matsu'ura 1977a,b; Loveless & Meade 2010; Avouac et al. 2014; Jolivet et al. 2014). It, however, entails a mechanical difficulty of artificial stress infinity at subfault edges (Romanet et al. 2020, 2024; Mallick & Meade 2025), and an issue of fault geometry inference is estimating macroscopic geometry, which is smooth, consistent with linear continuum mechanics (Matsu'ura et al. 2019). Distributed source inversions involving fault geometry inferences are proved to have solutions (Beretta et al. 2008; Volkov et al. 2017; Aspri et al. 2020; Diao et al. 2023), but how to solve them is under debate (Ragon et al. 2018; Dutta et al. 2021; Shimizu et al. 2021; Wei et al. 2023; Aspri et al. 2025).

This source geometry inference is entering a new phase owing to the potency density tensor inversion (PDTI, Kikuchi & Kanamori 1991; Kasahara & Yagi 2010; Shimizu et al. 2020), which reveals macroscopic fault geometry as spatially smooth rotations of estimated potency tensors. A seminal research of Kikuchi & Kanamori (1991) first infers a seismic source as inelastic strain (potency) distributed over a quasi-surface instead of as displacement discontinuity across a literal face. Nonetheless, their original PDTI is indistinct from planar fault subdivision and similar to multiple point source approaches (Tsai et al. 2005; Yue & Lay 2020) because the prior constraint they employ is only the assumption of double-coupling potency imposed as a traceless and determinant-free constraint. A fine

benefit of the PDTI comes from a prior constraint upon the fault geometry, which is, to our knowledge, first introduced by Kasahara & Yagi (2010). Smoothly varying macroscopic rotations of focal mechanisms are thus extracted by simply using a smoothness constraint on the model parameter in the PDTI. Kasahara & Yagi (2010) have further developed a stable scheme by accounting for the propagation of Green's function errors (Yagi & Fukahata 2010, 2011). Whereas the original intention of Kasahara & Yagi (2010) was rather to extract spatial variations in slip vectors and focal mechanisms themselves, Shimizu et al. (2020) point out that spatial patterns of the potency beachball diagram also document fault geometry as fault normal vector fields. The PDTI untangles source complexities in the perspective of fault geometry thereafter (Okuwaki et al. 2020; Tadapansawut et al. 2021; Fan et al. 2022; Ohara et al. 2023; Yagi et al. 2024; Inoue et al. 2025).

This natural extension of focal mechanism determination thus nearly establishes a methodology in which the macroscopic source geometry is immediately visualized as distributed potency beachballs. Shimizu et al. (2021) were able to estimate the fault geometry by further computing the normal vector ( $n$ -vector) estimate, which is given by one nodal plane of estimated potency, and spatially integrating estimated fault slopes given by the 90-degree rotations of  $n$ -vectors. However, the surface reconstruction procedure in Shimizu et al. (2021) cannot represent more than quasi-two-dimensional properties such as uniaxial bends and uniaxial twists. In fact, such a limitation stems from the seemingly harmless approach of constructing an optimum fault surface as an integral of optimum fault slopes. We show below that a fault slope field expected from the estimated  $n$ -vector field is generally not integrable in three dimensions no matter how precise the observations are, and so that the key to inferring an earthquake fault as a macroscopic smooth surface is the stochastic inference of fault shape.

## 2 PROBLEM SETTING OF EARTHQUAKE FAULT RECONSTRUCTION FROM DISTRIBUTED POTENCY

### 2.1 Forward model

Source geometry inference consists of the following three model equations.

The first model equation is the representation theorem for linear continua. Displacements  $u_i$  of data components  $i$  are expressed by linear combinations of potency areal densities  $D(\boldsymbol{\xi})$  at coordinates  $\boldsymbol{\xi}$  on faults  $\Gamma$  (Kikuchi & Kanamori 1991):

$$u_i = \int_{\Gamma} d\Sigma(\boldsymbol{\xi}) G_i(\boldsymbol{\xi}) D(\boldsymbol{\xi}), \quad (1)$$

where  $G_i(\boldsymbol{\xi})$  denotes Green's function relating  $u_i$  and  $D(\boldsymbol{\xi})$ . The same formulation of geometry infer-

ence applies to time-dependent problems, and we drop time dependence until our teleseismic applications.

The second model equation is the transformation of double couple sources to fault slips. When the potency density  $D$  is double-coupled, it is expressed by the symmetrized tensor product of a slip vector  $\mathbf{s}$  and a fault normal  $\mathbf{n}$ :

$$D = \frac{1}{2}(\mathbf{n}\mathbf{s}^T + \mathbf{s}\mathbf{n}^T), \quad (2)$$

where the superscript  $T$  denotes the transpose. Equation (2) tells that an  $n$ -vector is either of the nodal planes of potency in the beachball diagram standard in seismic moment representations. It is equivalent to one of the normalized sums of the maximum and minimum eigenvectors of  $D$ , accounting for the sign reversals of these eigenvectors. In this paper, we suppose that the normal  $n^\circ$  for a point source solution (e.g., the first-motion solution) is known and assume that the  $n$ -vector for  $D$  is its closest nodal plane to  $n^\circ$ . That is, the tilt of the  $n$ -vector from the reference is assumed to be within 45 degrees. Increasing the number of reference point sources may satisfy this assumption. Note that seismic moment is ill-defined in a strict sense across a stiffness discontinuity (e.g., a plate boundary), but potency is well-defined even across it.

The source inversion via eq. (1) and the nodal-plane extraction by eq. (2) have established methods of analysis. The potency density tensor inversion of eq. (1) is similar to the slip inversion (Yabuki & Matsu'ura 1992; Yagi & Fukahata 2011). The nodal-plane extraction of eq. (2) is the same as that for moment beachballs.

What remains is the correspondence between  $n$ -vectors and shapes of surfaces, and it is given by the definition of the  $n$ -vector: the normal vector  $\mathbf{n}(\boldsymbol{\xi})$  at a coordinate  $\boldsymbol{\xi}$  on a surface  $\Gamma$  is orthogonal to the infinitesimal shift  $d\boldsymbol{\xi}$  along  $\Gamma$  at  $\boldsymbol{\xi}$  as

$$\mathbf{n}(\boldsymbol{\xi}) \cdot d\boldsymbol{\xi}(\boldsymbol{\xi}) = 0. \quad (3)$$

In this paper, a ‘smooth surface’ denotes a surface whose shape is defined by eq. (3), known as a ‘regular surface’ in differential geometry. The orthogonality to the tangential plane defines the normal vector of the curved surface, and a relative location between two arbitrary points on a smooth surface is given by the line integral  $\int d\boldsymbol{\xi}$  that satisfies eq. (3). Since the  $n$ -vector field is equivalent to the shape of the smooth surface excepting its rigid-body translation, it entirely records the macroscopic smooth shape of a fault. Hereafter, one location  $\boldsymbol{\xi}^\circ$  on (or at least adjacent to) the fault (e.g., the rupture initiation point) is assumed to be known, and its estimation errors are neglected.



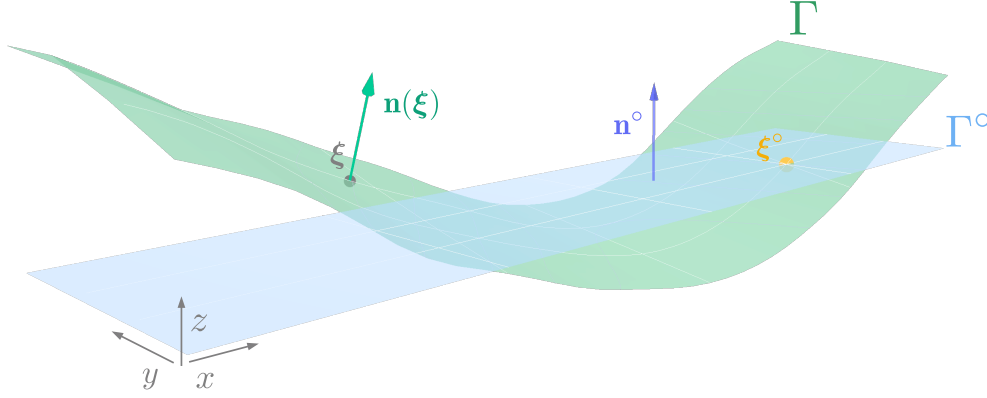


**Figure 1.** Parametrization of a fault surface  $\Gamma$  using a reference surface  $\Gamma^\circ$ . The normal vector  $\mathbf{n}$  of  $\Gamma$  depends on the location  $\boldsymbol{\xi}$  on  $\Gamma$  parametrized by  $(x, y, z)$ . The  $x$ - $y$  plane describes the coordinate of  $\boldsymbol{\xi}$  along  $\Gamma^\circ$ , and the  $z$  axis represents the vertical elevation of  $\Gamma$  from  $\Gamma^\circ$ . In the schematic,  $\Gamma^\circ$  is drawn as a flat face perpendicular to a reference vector  $\mathbf{n}^\circ$  through a point  $\boldsymbol{\xi}^\circ$  on  $\Gamma$ .

## 2.2 Detachment of surface reconstruction from potency estimation

Let us suppose that the potency density  $D$  and the associated  $n$ -vector field are evaluated given the well-known equations (1) and (2). Our focus is on how to translate them into  $\Gamma$  through eq. (3). However, the domain of definition for the observed potency density  $D$  depends on the fault shape  $\Gamma$  (eq. 1). To perform the inference of  $D$  prior to reconstructing  $\Gamma$ , the representation theorem (eq. 1) must be projected onto some fixed surface, termed the reference surface  $\Gamma^\circ$  (Fig. 1).

We now introduce  $\Gamma^\circ$  as a flat plane perpendicular to  $\mathbf{n}^\circ$  passing through  $\boldsymbol{\xi}^\circ$  (Shimizu et al. 2020, also see Fig. 1); if necessary, multiple flat planes are incorporated. Coordinates  $\boldsymbol{\xi}$  on  $\Gamma$  are parametrized as a function of the location  $(x, y)$  taken on  $\Gamma^\circ$  and the elevation  $z$  of  $\Gamma$  from  $\Gamma^\circ$ . The positive direction of  $z$  is directed to  $\mathbf{n}^\circ$ . Then, basis function expansions are applied to the potency density by using basis functions that depend only on  $(x, y)$ . The  $q$ -component  $D_q$  of the potency density tensor is expressed by bases  $X_j(x, y)$  ( $j = 1, \dots, M$ ), and the coefficients are stored in a vector  $\mathbf{a}$  as  $a_{j+(q-1)M}$ :

$$D_q(\boldsymbol{\xi}, \tau) = \sum_{j=1}^M a_{j+(q-1)M} X_j(x, y). \quad (4)$$

Substituting it into eq. (1), we have

$$u_i = H_{ij}(\Gamma) a_j, \quad (5)$$

where  $H_{ij}(\Gamma) = \int_{\Gamma} d\Sigma G_i(\boldsymbol{\xi}) X_j(x, y)$ . Note the domain of the surface integral of  $H_{ij}(\Gamma)$  is still the unknown  $\Gamma$ . In the PDTI,  $H_{ij}(\Gamma)$  is regularly approximated by a known surface  $\Gamma'$  (e.g.,  $\Gamma^\circ$ ) or an estimate  $\hat{\Gamma}$  [i.e.,  $H(\Gamma) \simeq H(\hat{\Gamma})$ , see §6.1 for details]. In the above manner, the object to simultaneously estimate (fault potency and fault geometry) is decomposed into model parameters  $\mathbf{a}$  and  $\Gamma$ . They are

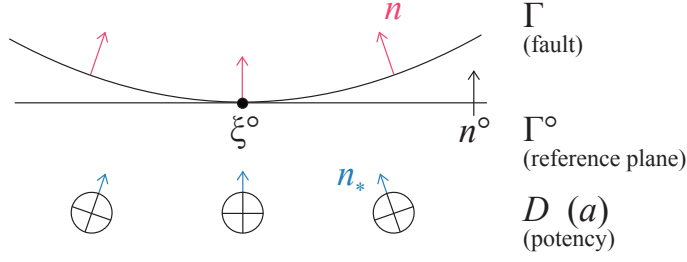


**Figure 2.** Three normal vectors determined by different fault properties, indicated by arrows of different colors. (Red) The normal vector  $n$  field of a fault shape  $\Gamma$ . (Black) The reference normal  $n^\circ$  for the reference surface  $\Gamma^\circ$ . (Blue) The normal vector  $n$  field corresponding to the potency  $D$  (precisely, that after a basis function expansion along the reference surface,  $a$ ).

formally independent in the above formulation, and their dependencies are described by an additional constraint, which is the theme of this study.

### 3 HOW TO MAP A POTENCY DENSITY ONTO A FAULT SHAPE

The translation of  $\mathbf{a}$  to express a potency distribution into a fault surface  $\Gamma$  requires a function  $f$  such that  $\Gamma = f(\mathbf{a})$ . When a potency density provides an  $n$ -vector field, the function to be sought is one that transforms the  $n$ -vector field into a surface shape. We formulate it in this section. Such a function corresponds to the inverse of eq. (3) mapping a surface  $\Gamma$  onto an  $n$ -vector field.

When eq. (3) holds, the relative displacement on  $\Gamma$ , namely the fault shape, is equivalent to the field of  $\mathbf{n}$ . At the same time, the tensor shape of the potency  $D$  dictates  $\mathbf{n}$  (eq. 2). Namely,  $\mathbf{n}$  is doubly characterized by  $\Gamma$  and  $D$  (Fig. 2). Those two are naively equal: articulating the  $n$ -vector defined by  $\Gamma$  as  $\mathbf{n}(\boldsymbol{\xi}; \Gamma)$  and the  $n$ -vector defined by  $D$  by  $\mathbf{n}_*(\boldsymbol{\xi}; \mathbf{a})$ ,

$$\mathbf{n}(\boldsymbol{\xi}; \Gamma) = \mathbf{n}_*(\boldsymbol{\xi}; \mathbf{a}). \quad (6)$$

Equation (6) is an absolute requirement in the conventional slip inversion, where  $\Gamma$  is defined first and  $\mathbf{n}(\boldsymbol{\xi}; \Gamma)$  of  $\Gamma$  constrains  $\mathbf{n}_*(\boldsymbol{\xi}; \mathbf{a})$ , the tensorial shape of the potency (e.g., Fukahata & Wright 2008; Dutta et al. 2021). In the framework of the PDTI, which permits general inelastic strains beyond the displacement discontinuity representation, the inelastic strain is expressed as the potency  $D$  first, and  $\mathbf{n}_*(\boldsymbol{\xi}; \mathbf{a})$  of  $D$  provides the information of  $\mathbf{n}(\boldsymbol{\xi}; \Gamma)$  via eq. (6).

Based on this theoretical relationship (eq. 6), Shimizu et al. (2021) have reconstructed  $\Gamma$  from the potency  $\mathbf{a}$  parametrized along a reference plane. The following equation is useful to transform the  $n$ -vector field to the surface; eq. (3) describes the infinitesimal in  $z$  attending the infinitesimal in

$\alpha = x, y,$

$$z_{,\alpha} = -n_{\alpha}/n_z, \quad (7)$$

where the subscript following a comma denotes the partial derivative. The elevation  $z$  is a single-valued function of  $x$  and  $y$  since we have limited the discussion to the case where the  $n$ -vector lies within 45 degrees from  $n^\circ$  for guaranteeing the unique conversion from potency tensors to  $n$ -vectors (§2.1).

Equation (7) states that the cotangent of the  $n$ -vector coincides with the downward gradient of a curve in a two-dimensional space, and the slip direction perpendicular to the  $n$ -vector is exactly the fault orientation in two dimensions. Hence, Shimizu et al. (2021) averaged the potency along the short side of the reference surface and smoothly connected the resulting  $n$ -vector along the long side to extract two-dimensional geometrical features of a uniaxially bended fault (e.g., along-strike strike angle variations and along-dip dip angle variations). The same procedure could generate quasi-two-dimensional shapes including uniaxial twists such as along-strike dip variations and along-dip strike variations (§5.3). This paper counts such quasi-two-dimensional shape reconstruction as the previous method by Shimizu et al. (2021).

However, three-dimensional surface reconstruction is beyond the scope of the method of Shimizu et al. (2021), which is ascribed to the difference in the degrees of freedom of  $n$ -vectors between two and three dimensions. In two dimensions, the  $n$ -vector may be expressed by the polar angle  $\theta$ . The transformation of a given  $n$ -vector field to an elevation  $z$  field is then a one-to-one mapping  $\theta \mapsto z$ , which provides a unique  $z$  field to an arbitrary smooth  $n$  field. By contrast, in three dimensions, the  $n$ -vector may be expressed by the polar angle  $\theta$  and the azimuthal angle  $\phi$ . Three-dimensional surface reconstruction from the  $n$ -vector is therefore a two-to-one mapping  $(\theta, \phi) \mapsto z$  from a vector field of  $\theta$  and  $\phi$  to a scalar field of  $z$ , generally having no solutions for eqs. (6) and (7) unless the given  $n$ -vector field is error-free. Namely, the surface reconstruction from potency is an overdetermined problem in three dimensions.

Its inverse, the one-to-two mapping of  $z$  on  $(\theta, \phi)$ , is precisely the definition of the normal vector simplified as eq. (7), and it is made bijective by the smoothness of the surface. A smooth surface with no tears, the aforementioned regular surface, sets a closed-path integral of relative elevation to zero:

$$\oint d\mathbf{l} \cdot \nabla z = 0, \quad (8)$$

where  $\nabla = (\partial_x, \partial_y)$  denotes the two-dimensional partial differential operator. From Stokes' theorem, it is expressed as

$$\int d\Sigma \nabla \times \nabla z = 0, \quad (9)$$

that is,

$$\partial_x \partial_y z = \partial_y \partial_x z. \quad (10)$$

Under this constraint on  $z$  by eq. (10), the one-to-two mapping of  $z$  on  $(\theta, \phi)$  becomes bijective. Equation (10) indicates that the requirement of the smooth surface with no tears is that  $\nabla z$  is integrable, that is, the elevation  $z$  is a continuous function with no jumps. Quasi-two-dimensional surface reconstruction is an approximation that neglects that the slope along the long side may vary along the short side (e.g.  $\partial_y z_{,x} \simeq 0$ ), so it violates eq. (10) when the slope along the short side varies along the long side (e.g.  $\partial_x z_{,y} \neq 0$ ).

Substituting eq. (7) into eq. (10) leads to

$$\partial_x (n_y/n_z) = \partial_y (n_x/n_z). \quad (11)$$

Two-dimensional shapes of uniaxial bending (single-curved surfaces) treated in Shimizu et al. (2021) always set both sides of eq. (11) equally to zero. However, only the error-free  $n$ -vector field of a surface meets eq. (11) in three dimensions. Other than such special cases, the estimated normal vectors of curved surfaces violate the integrability condition of eq. (11), and that is the reason why the  $(\theta, \phi) \mapsto z$  mapping of eqs. (6) and (7) is overdetermined:

$$\partial_x (n_{*y}/n_{*z}) \neq \partial_y (n_{*x}/n_{*z}). \quad (12)$$

Since the source surface reconstruction via eqs. (6) and (7) is overdetermined and eq. (7) is the identity of the normal vector of a surface, surface reconstruction from given potency must read eq. (6) as some projection:

$$n(\xi; \Gamma) \xrightarrow{\mathcal{P}} n_*(\xi; \mathbf{a}), \quad (13)$$

where  $\xrightarrow{\mathcal{P}}$  denotes some operation to remove non-integrable components such that  $\partial_x (n_{*y}/n_{*z}) \neq \partial_y (n_{*x}/n_{*z})$ . Only if that non-integrable portion of  $n_*$  is removed, that is, only if illogical tears are ruled out, a fault is reconstructed as a smooth surface in a coarse-grained continuum.

Because  $n \mapsto z$  mapping is impossible when the theoretical relationship between potency and shape of eq. (6) strictly holds, surface reconstruction from potency must loosen this premise. There remains, however, arbitrariness in eq. (13) on how that loosening is applied. We describe this subjective postulation as prior information. Equation (13) expects that the  $n$ -vector  $\mathbf{n}(\xi, \Gamma)$  of a surface  $\Gamma$  approaches the  $n$ -vector  $\mathbf{n}_*(\mathbf{a})$  (defined by eq. 2) pointed by the nodal planes of potency beachballs. The constraint of approximating a normalized vector to a designated value yields a non-Gaussian central-limit distribution known as the von Mises-Fisher distribution; it measures the distance of vectors by

the inner product, and for a uniform isotropic case,

$$P(\Gamma|\mathbf{a}; \kappa) = \exp[\kappa \int_{\Gamma} d\Sigma(\boldsymbol{\xi}) \mathbf{n}_*(\boldsymbol{\xi}, \mathbf{a}) \cdot \mathbf{n}(\boldsymbol{\xi}, \Gamma)] / \mathcal{Z}, \quad (14)$$

where  $\kappa$  denotes a scale factor, and  $\mathcal{Z}$  is a normalization constant. The domain of integration is set to  $\Gamma$ , and  $P(\Gamma|\mathbf{a}; \kappa)$  is independent of the way to take the reference surface  $\Gamma^\circ$ .

Then, eq. (13) requires the limit that places  $\mathbf{n}$  in the integrable nearest neighbor of non-integrable  $\mathbf{n}_*$ , that is, the displacement discontinuity that best approximates given inelastic strain. It is termed dislocation limit hereafter, which is, in eq. (14),

$$\kappa \rightarrow \infty. \quad (15)$$

In this limit,

$$P(\Gamma|\mathbf{a}) = \delta(\Gamma - \Gamma_*(\mathbf{a})), \quad (16)$$

where  $\delta(\cdot)$  denotes Dirac delta and

$$\Gamma_* := \operatorname{argmax}_{\Gamma|\mathbf{a}} P(\Gamma|\mathbf{a}; \kappa). \quad (17)$$

Here  $\operatorname{argmax}$  denotes the arguments of the maxima. In this paper,  $P(\Gamma|\mathbf{a})$  is taken as  $\lim_{\kappa \rightarrow \infty} P(\Gamma|\mathbf{a}, \kappa)$ .

When  $(\partial_x \partial_y - \partial_y \partial_x)z$  expected from  $n_*$  is small,  $n$  obtained from eq. (13) is not so shifted from  $n_*$ . Basically, we suppose such cases and proceed by assuming  $P(\Gamma|\mathbf{a})$  of eq. (14). However, the overdetermination of surface reconstruction, in which any surface cannot obey the forward model eq. (2) that yields eq. (6), leaves open the question of what priors  $P(\Gamma|\mathbf{a})$  are appropriate to loosen eq. (2) when  $(\partial_x \partial_y - \partial_y \partial_x)z$  of  $n_*$  is not small. Even before the  $n$ -vector is disturbed by measurement errors that do not satisfy eq. (6), the fault face as an earthquake source is an approximation of a fracture zone, which accounts for the nature of brittle failure that localizes within a quasi-face (Matsu'ura et al. 2019), so the exact observance of eq. (2) is originally unphysical. Thus, if read as a forward model prior to the observation,  $P(\Gamma|\mathbf{a})$  for returning a surface from a given  $n$ -vector field is a probabilistic delineation of the ambiguity of an earthquake fault, an idealization of a thin sheet of inelastic deformation.  $P(\Gamma|\mathbf{a})$  is different from the posterior probability of fault shape. The  $n$ -vector-geometry mapping, and therefore the surface reconstruction of earthquake faults from potency, are never beyond Bayesian probabilistic even when potency is given deterministically, and the posterior of fault shape is the convolution between the conditional prior of fault shape given potency  $P(\Gamma|\mathbf{a})$  and the posterior of potency (Appendix A).

#### 4 AN ANALYTIC SOLUTION FOR $\Gamma_*$ AS THE OPTIMAL ELEVATION FIELD

It has been shown inevitably probabilistic to project two degrees of freedom in the expected normal  $n_*$  onto one degree of freedom in the smooth surface elevation. Bearing  $P(\Gamma|\mathbf{a})$  of eq. (14) in mind, we derive an analytical expression of the most probable surface estimate  $\Gamma_*(\mathbf{a})$  given the potency  $\mathbf{a}$ . This section assumes that the non-integrable component of  $n_*$  (eq. 12) is small so that the solution of surface reconstruction does not depend much on the functional form of  $P(\Gamma|\mathbf{a})$ .

We have supposed that the potency density  $\mathbf{a}$  uniquely determines the field of the normal vector  $n_*$  (§2.1), so the goal of this section is to obtain  $\Gamma_*$  given  $n_*$ . When the  $x$ - $y$  plane describes the location along the reference surface  $\Gamma^\circ$ ,  $\Gamma$  is parametrized by  $z(\cdot, \cdot)$ , which represents the elevation of  $\Gamma$  from  $\Gamma^\circ$  as a function of the position along the reference surface  $(x, y)$ .

##### 4.1 Governing equation

The governing equation of the problem is now the definitional identity of the  $n$ -vector (eq. 7). It indicates the orthogonality between the  $n$ -vector and a curved surface, which in three dimensions means more than that a 90-degree rotation (cotangent) of the  $n$ -vector gives the downward surface slope; introducing

$$n_\perp = \sqrt{n_x^2 + n_y^2} \quad (18)$$

$$\mathbf{n}_\parallel = (n_x, n_y)/n_\perp, \quad (19)$$

we can rewrite eq. (7) as

$$\nabla z = -\frac{n_\perp}{n_z} \mathbf{n}_\parallel. \quad (20)$$

Namely, the  $n$ -vector indicates the direction of the slope by its horizontal projection  $\mathbf{n}_\parallel$  ( $|\mathbf{n}_\parallel| = 1$ ) as well as the downward slope by its horizontal-vertical ratio  $n_\perp/n_z$  (Fig. 3).

The remaining analysis is straightforward when the  $n$ -vector is parametrized in a spherical coordinate. Now the polar angle  $\theta \in [0, \pi]$  is set as the angle between  $\mathbf{n}^\circ$  and  $\mathbf{n}$ , and the azimuthal angle  $\phi \in [0, 2\pi)$  is measured from the  $x$  axis. For this setting,

$$\begin{aligned} n_z &= \cos \theta \\ n_\perp &= \sin \theta \\ n_{\parallel x} &= \cos \phi \\ n_{\parallel y} &= \sin \phi. \end{aligned} \quad (21)$$

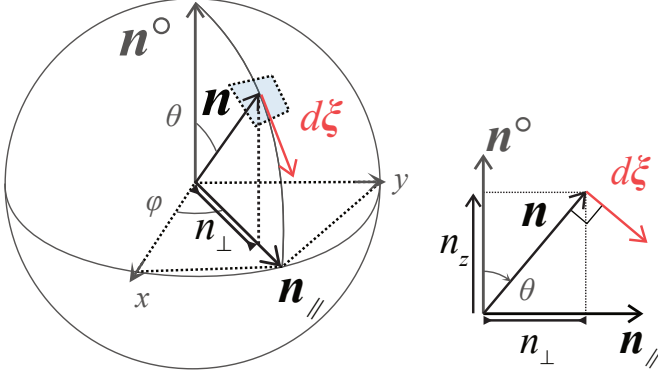


**Figure 3.** Details of the orthogonality between the  $n$ -vector  $\mathbf{n}$  and the tangent plane  $d\xi$  of a surface. A Cartesian coordinate is introduced such that the reference-surface normal  $\mathbf{n}^\circ$  points to the  $z$  axis, and  $x$  and  $y$  represent the location along the reference surface. The surface slope direction is indicated by the horizontal projection  $\mathbf{n}_\parallel$  of  $\mathbf{n}$ . The downward surface slope coincides with the ratio of the horizontal component  $n_\perp$  to the vertical component  $n_z$  of  $\mathbf{n}$ .

Note  $n_x = \sin \theta \cos \phi$  and  $n_y = \sin \theta \sin \phi$ . Plugging eq. (21) into eq. (20),

$$\nabla z = -\tan \theta \begin{pmatrix} \cos \phi \\ \sin \phi \end{pmatrix}. \quad (22)$$

Hereafter, the basis vectors for the position  $(\theta, \phi)$  on a unit sphere pointing toward  $\mathbf{n}$  are denoted as  $\mathbf{n}$  (along the  $n$ -vector),  $\mathbf{e}_\theta$  (parallel to the  $\theta$  axis), and  $\mathbf{e}_\phi$  (parallel to the  $\phi$  axis).

## 4.2 Solving a stochastic partial differential equation for fault elevation

The shape of  $\Gamma$  is equivalent to both the  $z$  field and the  $n$  field, but formally, eq. (7) can be read as a partial differential equation of  $z$  with a random external force  $-(n_\perp/n_z)\mathbf{n}_\parallel$  imposed. The probability  $P(\Gamma|\mathbf{a}; \kappa)$  (eq. 14) describes fluctuations of the  $n$ -vector from the expectation  $n_*$ . We derive an analytical solution of this stochastic partial differential equation. For this derivation, we assume non-integrable components (eq. 12) of  $n_*$  are small; the full-order derivation becomes complicated (Appendix B).

First, we rewrite the Cartesian forms of  $P(\Gamma|\mathbf{a}; \kappa)$  (eq. 14) and the partial differential equation of the elevation (eq. 7) in the spherical coordinate. In a spherical coordinate system at a unit spherical position  $(\theta_*, \phi_*)$  of  $\mathbf{n}_*$ ,  $\mathbf{n}$  is expressed as

$$\mathbf{n} = \chi_n^* \mathbf{n}_* + \chi_\theta^* \mathbf{e}_\theta + \chi_\phi^* \mathbf{e}_\phi, \quad (23)$$

with associated coefficients  $(\chi_n^*, \chi_\theta^*, \chi_\phi^*)$ . The first order of the Taylor series with respect to angle

fluctuations  $\theta - \theta_*$  and  $\phi - \phi_*$  around  $n_*$  yields

$$\begin{aligned}\chi_\theta^* &= (\theta - \theta_*) + \mathcal{O}(\delta\Omega^2) \\ \chi_\phi^* &= (\phi - \phi_*) \sin \theta_* + \mathcal{O}(\delta\Omega^2),\end{aligned}\tag{24}$$

where  $\mathcal{O}(\delta\Omega^k)$  denotes the  $k$ -th order angle fluctuations from  $n_*$ . Note  $\partial \mathbf{n}(\theta, \phi)/\partial \theta = \mathbf{e}_\theta$  and  $\partial \mathbf{n}(\theta, \phi)/\partial \phi = \mathbf{e}_\phi \sin \theta$ . The normalization condition  $\mathbf{n} \cdot \mathbf{n} = 1$  of  $\mathbf{n}$  and the above expressions of  $\chi_\theta^*$  and  $\chi_\phi^*$  result in

$$\chi_n^* = 1 - [(\theta - \theta_*)^2 + (\phi - \phi_*)^2 \sin^2 \theta_*]/2 + \mathcal{O}(\delta\Omega^3).\tag{25}$$

Therefore, for the von Mises-Fisher distribution of eq. (14), we have

$$\mathbf{n}_* \cdot \mathbf{n} = 1 - [(\theta - \theta_*)^2 + (\phi - \phi_*)^2 \sin^2 \theta_*]/2 + \mathcal{O}(\delta\Omega^3)\tag{26}$$

and

$$P(\Gamma|\mathbf{a}; \kappa) = \exp\left\{-\frac{\kappa}{2} \int_\Gamma d\Sigma [(\theta - \theta_*)^2 + (\phi - \phi_*)^2 \sin^2 \theta_* + \mathcal{O}(\delta\Omega^3)]\right\} / \mathcal{Z},\tag{27}$$

where  $\mathcal{Z}'$  represents normalization. Only the second-order fluctuations from  $n_*$  matter in the dislocation limit  $\kappa \rightarrow \infty$  if non-integrable components (eq. 12) of  $n_*$  are small.

We next evaluate the partial differential equation of the elevation (eq. 7), which is expressed as eq. (22) in the spherical coordinate. The Taylor series of eq. (22) in angle fluctuations from  $n_*$  leads to

$$\nabla z = \nabla z_* - \cos^{-2} \theta_* \begin{pmatrix} \cos \phi_* \\ \sin \phi_* \end{pmatrix} (\theta - \theta_*) - \tan \theta_* \begin{pmatrix} -\sin \phi_* \\ \cos \phi_* \end{pmatrix} (\phi - \phi_*) + \mathcal{O}(\delta\Omega^2),\tag{28}$$

where  $z_{*,\alpha} := -n_\alpha/n_z$ . Using eq. (21) again and taking the inner and cross products of  $\nabla z$  and  $\mathbf{n}_{*\parallel}$ , we find

$$\theta - \theta_* = -n_{*z}^2 \mathbf{n}_{*\parallel} \cdot (\nabla z - \nabla z_*) + \mathcal{O}(\delta\Omega^2)\tag{29}$$

$$\phi - \phi_* = -(n_{*z}/n_{*\perp}) \mathbf{n}_{*\parallel} \times (\nabla z - \nabla z_*) + \mathcal{O}(\delta\Omega^2),\tag{30}$$

or explicitly, recalling  $\mathbf{n}_\parallel \cdot \nabla z = -n_\perp/n_z$  and  $\mathbf{n}_\parallel \times \nabla z = 0$  (eq. 20),

$$\theta - \theta_* = -n_{*z}^2 (n_{*\parallel x} z_{*,x} + n_{*\parallel y} z_{*,y} + n_{*\perp}/n_{*z}) + \mathcal{O}(\delta\Omega^2)\tag{31}$$

$$\phi - \phi_* = -n_{*\perp}^{-1} n_{*z} (n_{*\parallel x} z_{*,y} - n_{*\parallel y} z_{*,x}) + \mathcal{O}(\delta\Omega^2).\tag{32}$$

Plugging eqs. (31) and (32) into  $P(\Gamma|\mathbf{a})$  (eq. 27 with  $\kappa \rightarrow \infty$ ), we arrive at

$$\begin{aligned}\ln[P(\Gamma|\mathbf{a}) \times \mathcal{Z}'] &= -\frac{\kappa}{2} \left\{ \int_\Gamma d\Sigma [n_{*z}^2 (n_{*\parallel x} z_{*,x} + n_{*\parallel y} z_{*,y} + n_{*\perp}/n_{*z})]^2 \right. \\ &\quad \left. + \int_\Gamma d\Sigma [n_{*z} (n_{*\parallel x} z_{*,y} - n_{*\parallel y} z_{*,x})]^2 + \mathcal{O}(\delta\Omega^3) \right\}.\end{aligned}\tag{33}$$



Here  $\sin \theta = n_\perp$  (eq. 21) is also used. The area element  $d\Sigma(\boldsymbol{\xi})$  along the fault is larger than the area element  $dx dy$  along the reference plane because of the tilt of the fault normal by  $\theta$ :

$$d\Sigma(\boldsymbol{\xi}) = \frac{dx dy}{|\cos \theta(\boldsymbol{\xi})|} = |n_z|^{-1} dx dy. \quad (34)$$

Note  $|n_z| = n_z$  for  $\theta$  below 45 degrees now considered. In the dislocation limit, with small non-integrable components (eq. 12) of  $n_*$ , the higher order fluctuations from  $n_*$  are dropped, and the most probable estimate  $\Gamma_*$  for given  $n_*$  is expressed as:

$$\Gamma_* = \operatorname{argmin} \left\{ \int |n_{*z}| (n_{*||x} n_{*z} z_{,x} + n_{*||y} n_{*z} z_{,y} + n_{*\perp})^2 dx dy + \int |n_{*z}| (n_{*||x} z_{,y} - n_{*||y} z_{,x})^2 dx dy \right\}, \quad (35)$$

where  $\operatorname{argmin}$  denotes the arguments of the minima. To avoid zero divisions at  $n_{*z} = 0$ ,  $n_{*z}^2$  among the weight  $|n_{*z}^3|$  in the first term was placed inside the brackets. The first term from the  $\theta$  fluctuation constrains the  $\mathbf{n}_{||}$ -parallel component of the fault slope  $\nabla z$ , and the second term from the  $\phi$  fluctuation constrains the  $\mathbf{n}_{||}$ -perpendicular component of  $\nabla z$ . Their weights  $|n_{*z}^3|$  and  $|n_{*z}|$  derive from the independence of  $P(\Gamma|\mathbf{a})$  from the reference plane orientation, and consequently, the constraints become weaker for steeper slopes (i.e., smaller  $n_{*z}$  for larger  $\theta(< \pi/4)$ :  $\partial n_{*z}/\partial \theta_* = -\sin \theta_* < 0$ ).

Thus, equations to be solved (eqs. 7 and 14) are reduced to a least square form of eq. (35). The rest of analysis is the ordinary linear inversion, which we omit to detail. We have solved it using a basis function expansion in this paper, instead of solving it in the continuous space, where the  $x$  and  $y$  derivatives of the  $n$ -vector appear, complicating implementations outside differentiable programming. The basis functions employed are the quadratic B-spline functions as in the PDTI, with intervals 1.5 times wider than that of the PDTI. The surface integral of the loss function is collocated at the  $x$ - $y$  positions of the spline knots adopted in the PDTI. We have removed the rigid-body translation of the fault by specifying a point with zero elevation. This translation of a fault is unconstrained in eq. (35) and does not affect fault elevations regardless of the way of removal.

The resultant estimation remains the least square using eqs. (31) and (32) even when generalizing  $P(\Gamma|\mathbf{a})$  to account for the expected elevation field  $\bar{z}$  such that

$$Q(\Gamma|\mathbf{a}) = \exp \left[ -\frac{1}{2} \int d\Sigma(\boldsymbol{\xi}) \int d\Sigma(\boldsymbol{\xi}') \begin{pmatrix} \theta(\boldsymbol{\xi}) - \theta_*(\boldsymbol{\xi}) \\ \phi(\boldsymbol{\xi}) - \phi_*(\boldsymbol{\xi}) \\ z(\boldsymbol{\xi}) - \bar{z}(\boldsymbol{\xi}) \end{pmatrix}^T \mathbf{w}(\boldsymbol{\xi}, \boldsymbol{\xi}') \begin{pmatrix} \theta(\boldsymbol{\xi}') - \theta_*(\boldsymbol{\xi}') \\ \phi(\boldsymbol{\xi}') - \phi_*(\boldsymbol{\xi}') \\ z(\boldsymbol{\xi}') - \bar{z}(\boldsymbol{\xi}') \end{pmatrix} \right] / \text{const.} \quad (36)$$

Our PDTI application includes such terms for computational acceleration (§6.2). The scope of eq. (36) covers a generalization using the probabilities of source locations, such as surface reconstruction from the locations and mechanisms of distributed point sources. It is also applicable to incorporating the

constraints on fault edge locations, such as accounting for fault surface traces and jointing multiple fault surfaces. Note  $P(\Gamma|\mathbf{a})$  other than eq. (14) is reduced to the quadratic form of eq. (36) when the higher orders are dropped. The explicit representation of those higher orders dropped in the dislocation limit is given by the non-perturbative expression of the  $n$ -vector as a function of  $\nabla z$  (eq. 37 in the next section).

## 5 SURFACE RECONSTRUCTION FROM SYNTHESIZED NOISY NORMAL VECTORS

We conduct synthetic tests of the most probable surface estimation (eq. 35) given the normal vector field. Simultaneous inference of potency density and geometry is often not significantly different from reconstructing fault geometry from the PDTI prescribing potency locations (Shimizu et al. 2021, also see §6.3). So this verification of surface reconstruction from a given noisy  $n$ -vector field serves the core verification of the PDTI involving fault shape inference, which is performed in §6.

A correct elevation  $z_0(x, y)$  perpendicular to the reference plane  $x$ - $y$  is first synthesized, and its normal vector field  $n_0(x, y)$  is given as  $n_*(x, y)$  disturbed by a noise  $\delta n(x, y)$ . From this noisy  $n_*(x, y)$ , we compute an estimate of the elevation  $\Gamma_*$  and check the accuracy compared to the correct shape. All components of the  $n$ -vector are disturbed by Gaussian random numbers of mean 0 and standard deviation  $\sigma_n$ , and their normalized values are taken as  $n_*$ . The  $n_*$  values are collocated on the grid points, and we assume that the grid interval is enough large to neglect spatial correlations for simplicity. The grid is the same as the knot configuration in the basis function expansion of the PDTI appearing in our application (§6.3). It is arranged with 40 points along strike  $x$  and 4 points along dip  $y$  spaced by 5 km, containing 160 points in total. The length scale in the following tests is nondimensionalized by setting km at unity.

The transformation of the fault slope to the fault normal in Cartesian coordinates is given by eq. (7) and the normalization condition  $|\mathbf{n}|^2 = 1$ :

$$\begin{aligned} n_z &= 1/\sqrt{1 + z_{,x}^2 + z_{,y}^2} \\ n_\alpha &= -z_{,\alpha}/\sqrt{1 + z_{,x}^2 + z_{,y}^2}. \end{aligned} \tag{37}$$

For spherical coordinates, from eq. (22),

$$\begin{aligned} \theta &= \text{atan}\sqrt{z_{,x}^2 + z_{,y}^2} \\ \phi &= \text{atan2}(z_{,y}, z_{,x}), \end{aligned} \tag{38}$$

where  $\text{atan2}(\cdot, \cdot)$  denotes 2-argument arctangent.

Two model shapes are considered. The first shape is a uniaxial twist (§5.1). It is accompanied with biaxial slopes, providing a simplest instance of a surface that is torn (i.e. eq. 11 is violated) if a uniaxial

interpolation is applied to the  $n$ -vector field. It is also an example of the surfaces that can be expressed by spline interpolation without interpolation errors, called developable surfaces. These make this geometry useful for method comparisons with the existing spline-interpolation-based approach (Shimizu et al. 2021). The second is a bowl shape (§5.2), which is an example of non-developable surfaces that intrinsically need stochastic reconstruction. A similar geometry is estimated in our case study of the 2013 Balochistan earthquake (§6.3). In both examples, the maximum horizontal component of the normal vector is approximately  $n_{\perp} = 0.45$ , and the normal vector is tilted by approximately 40 degrees from the reference plane. These are fairly curved shapes within the range where the conversion from potency beachballs to normal vectors is straightforward, that is within tilt angles of 45 degrees. There is little difference in the maximum normal between the two, but their reconstruction accuracies differ (§5.3).

Now we suppose  $\sigma_n < 0.25$ . Since fairly curved surfaces are computed, large noise results in  $n_z^* < 0$  ( $\theta > \pi/2$ ) outside the present problem setting. The  $n_z^* < 0$  condition is formally accounted for in the loss function of eq. (34), but our consideration following eq. (7) treats only the case of a single-valued  $z$  on the  $x$ - $y$  plane, where  $n_z^* \geq 0$  holds. The  $n$ -vector determination assuming the  $n$ -vector as the nodal plane closer to the reference has already assumed  $\theta < \pi/4$ , so  $\theta \geq \pi/4$  containing  $n_z^* < 0$  is supposed to be avoided in this study by setting multiple reference normals (§2.1). Stochastic surface reconstruction involving stochastic  $n$ -vector determinations is left open for future study.

### 5.1 A uniaxial twist

The first test treats the uniaxial twist shown in Fig. 4. Its elevation is symmetrical about the short side  $y$  (see Fig. 4 caption). Except for the center line  $y = 0$ , where  $n_x = 0$  identically, both  $n_x$  and  $n_y$  are non-zero, and the  $n$ -vector varies three-dimensionally. The two-dimensional visualization of the shape is a birds-eye view hereafter.

The estimation results with a noise standard deviation of 0.05 are indicated in Fig. 5. Despite that the input  $n$ -vectors are noisy, the estimated elevation is consistent with the original shape. Concavities and convexities at the four corners of the original shape are reproduced while the contours shift. As mentioned in the previous section, the noise component ( $\Delta n = n_* - n_0$ ) almost surely does not satisfy the slope integrability condition (eq. 11). Therefore, when  $n_*$  is disturbed from the  $n$ -vector of a surface, the most probable surface  $\Gamma_*$  (eq. 35) for given  $n_*$  could selectively remove the noise in  $n_*$ .

### 5.2 A bowl shape

The second test treats a bowl-shaped surface shown in Fig. 6, which is similar to the result of our actual data analysis concerning the 2013 Balochistan earthquake (§6.3). The elevation  $z$  is expressed by a

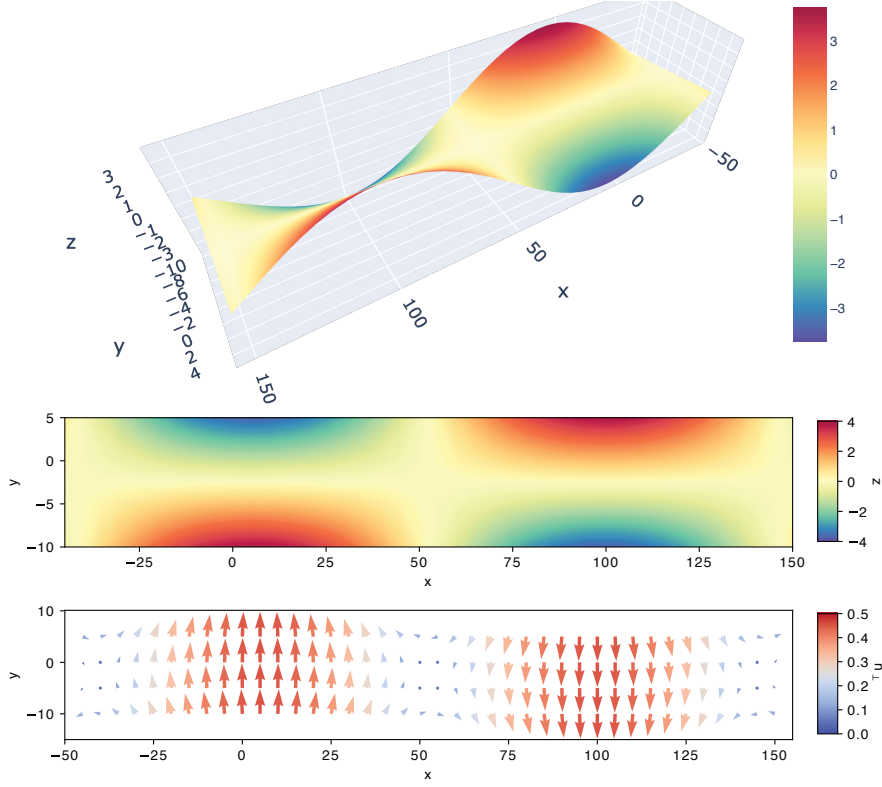


**Figure 4.** The ground truth of our synthetic test 1:  $z = [(y - \bar{y})/W] \sin[(x - \bar{x})/L]$  with  $W = 2$  and  $L = 30$ , where  $(\bar{x}, \bar{y})$  denotes the reference plane center.

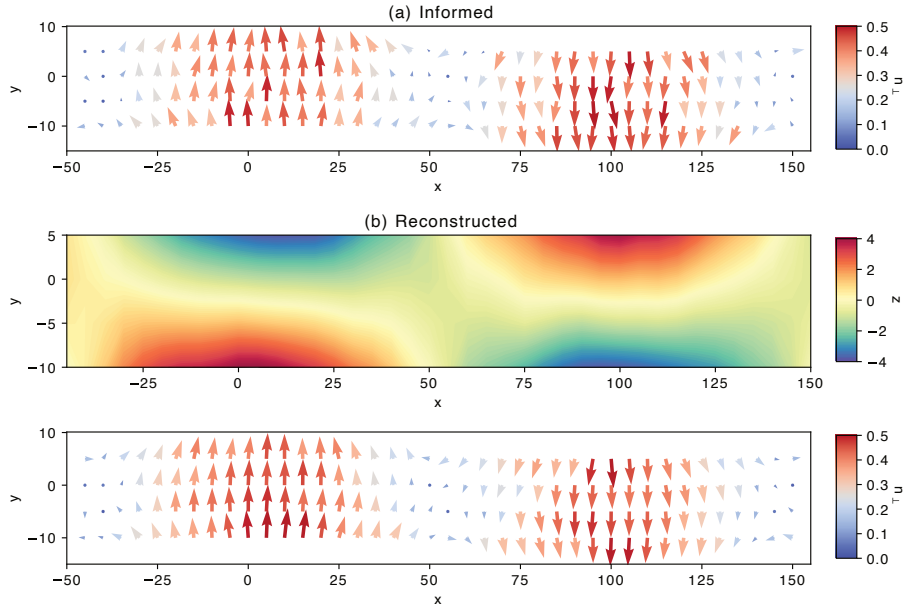


**Figure 5.** Examples of (a) informed noisy  $n$ -vectors and (b) reconstructed elevation and  $n$ -vector fields in our synthetic test 1. The  $n$ -vector randomly varies from the ground truth with a standard deviation of 0.05.

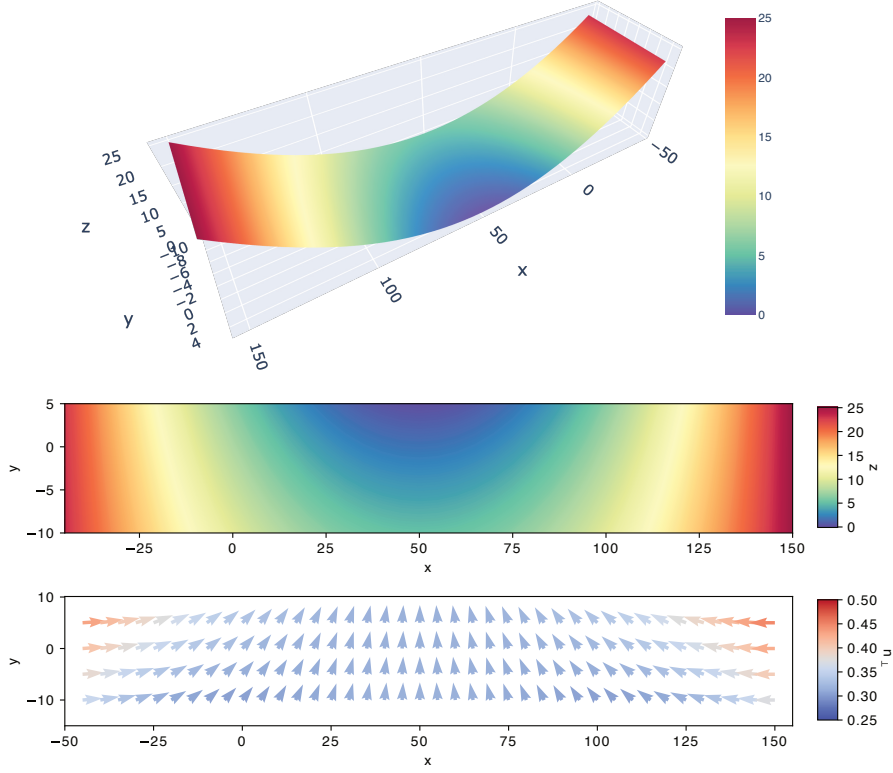


**Figure 6.** The ground truth of our synthetic test 2:  $z = -y/Y_1 + (x/X)^2(Y - Y_2)/Y_1$  with  $X = 50$ ,  $Y_1 = 3$ , and  $Y_2/Y_1 = -25$ .

function that is parabolic along the long side  $x$  and linear along the short side  $y$  (see Fig. 6 caption). When  $x$  is interpreted as the horizontal axis and  $y$  as the vertical, the surface horizontally bends well at the top and increases vertical tilts at the horizontal end (larger  $|z_{,x}|$  for larger  $y$  and larger  $z_{,y}$  for larger  $|x|$ , roughly speaking).

The results for a standard deviation of 0.05 are indicated in Fig. 7 as in the first test. The reconstructed shape seems more stable than the reconstructed uniaxial twist. This difference suggests that when the  $n$ -vector noise is at the same level, short-wavelength features such as topography are relatively susceptible to the  $n$ -vector noise. Considering that wider-regional elevations are controlled by longer-wavelength slopes, we ascribe this tendency to the spatial averaging that low-passes the slope error in a long-wavelength scale. The higher surface reproducibility at longer wavelengths might be reinforced in the application to the PDTI, to which the spatial potency smoothing is commonly applied.

### 5.3 Robustness tests of surface reconstruction

Figure 8 summarizes the errors and residuals of the above two tests with variable noise levels. The estimation errors  $1 - \hat{n} \cdot n_0$  and data residuals  $1 - \hat{n} \cdot n_*$  for normal vectors (Fig. 8a, b) are both linear

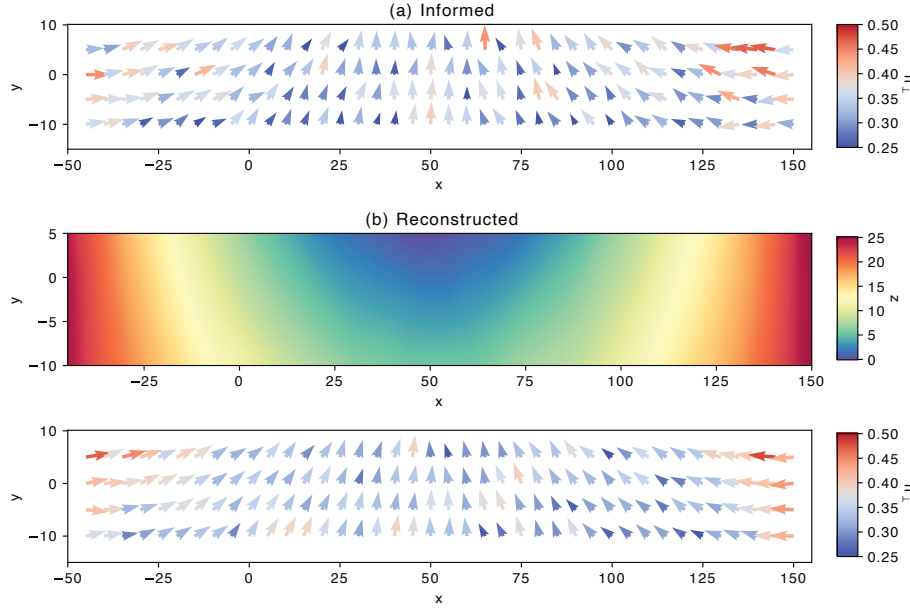


**Figure 7.** Examples of (a) informed noisy  $n$ -vectors and (b) reconstructed elevation and  $n$ -vector fields in our synthetic test 2. The  $n$ -vector randomly varies from the ground truth with a standard deviation of 0.05.

with the noise amplitude  $1 - n_0 \cdot n^*$ . The data residuals are visibly smaller than the noise amplitude, indicating significant variance reduction. The estimation error  $1 - \hat{n} \cdot n_0$  is smaller than the data residual  $1 - \hat{n} \cdot n_*$ , suggesting that the output denoises the given  $n$ -vector rather than explains it. The spatial average of elevation errors  $|z - \bar{z}|$  ( $\Gamma_*$  in Fig. 8c, d) is more scattered than that of normal vectors (Fig. 8a, b), and its average is roughly proportional to the square root of the noise amplitude of the normal vectors  $1 - n_0 \cdot n^*$  that approximates squared angle fluctuations. The elevation residuals are roughly the same between the two shapes (Fig. 8c, d), and these same-order absolute residuals indicate a significant difference in relative residuals, supporting higher reproducibility of a bowl-shaped curve compared to uniaxially twisting roughness observed in the previous subsections.

For comparison, we have also evaluated quasi-two-dimensional surface construction from Shimizu et al. (2021) (quasi 2D in Fig. 8c, d). It evaluates the elevation as  $z(x, y) \simeq z(\bar{x}, \bar{y}) + \int_{\bar{x}}^x dx' \bar{z}_{,x}(x') + \bar{z}_{,y}(x)(y - \bar{y})$  by using the mean slope  $\bar{z}_{,\alpha} = - \int dy (n_{\alpha}^*/n_z^*) / \int dy$  integrated over the short side  $y$ . We assume  $z(\bar{x}, \bar{y})$  at the reference plane center  $(\bar{x}, \bar{y})$  is known in this quasi-two-dimensional reconstruction. The stochastic surface reconstruction  $\Gamma_*$  works well as quasi-two-dimensional reconstruction for small noise, and for large noise, rather  $\Gamma_*$  has smaller estimation errors. Even for a uniaxial twist, for which quasi-two-dimensional approximation is errorless, the accuracy of  $\Gamma_*$  is higher, though the difference is less than accuracy variations (Fig. 8c). Meanwhile, for a bowl shape similar to the fault shape inferred in our application (§6.3), the accuracy of  $\Gamma_*$  is a few times greater than the quasi-two-dimensional benchmark for the maximum noise amplitude in this test (Fig. 8d).

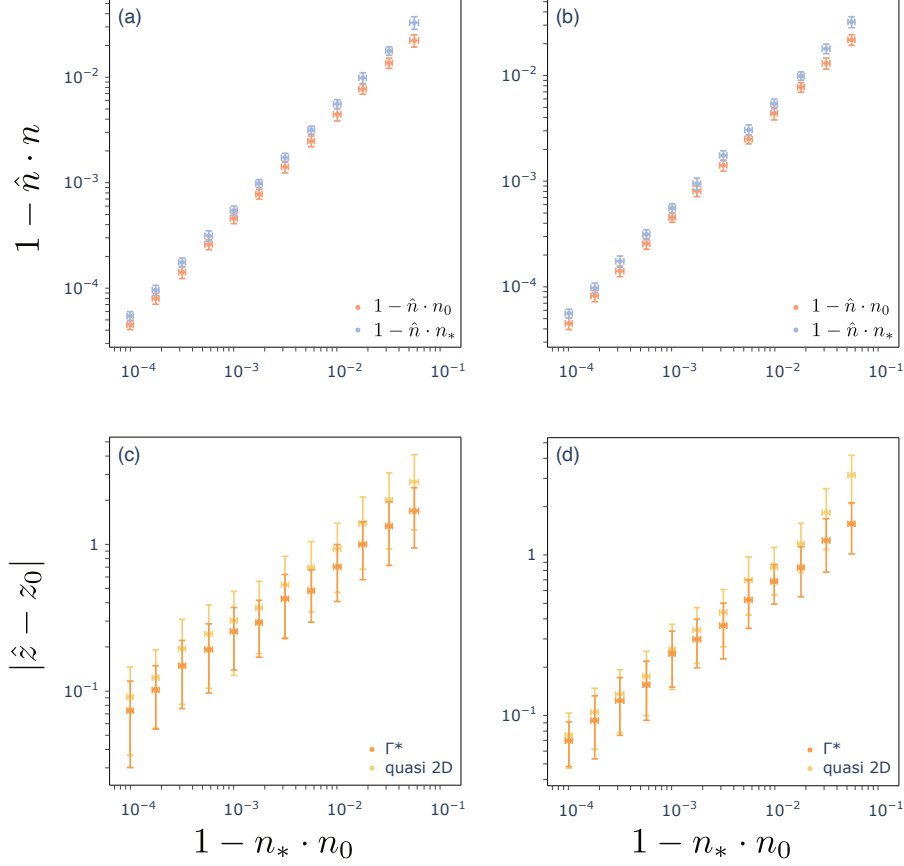


**Figure 8.** Errors and residuals in our synthetic tests, plotted in terms of  $n$ -vectors in tests 1 (a) and 2 (b) and elevations in tests 1 (c) and 2 (d). All values are averaged over the reference plane, and 64 noise patterns are used to evaluate the means and standard deviations shown in the panels. The horizontal axis  $1 - n_* \cdot n_0$  represents the noise level of input  $n$ -vectors  $n_*$  from the ground truth  $n_0$ . The vertical axis  $1 - \hat{n} \cdot n$  in (a) and (b) represents the errors  $1 - \hat{n} \cdot n_0$  (red) and the residuals  $1 - \hat{n} \cdot n_*$  (blue) of  $n$ -vector estimates  $\hat{n}$ . The vertical axis  $|\hat{z} - z_0|$  in (c) and (d) represents the error of estimated elevation  $\hat{z}$  from the ground truth  $z_0$  (orange). Elevation errors of quasi-two-dimensional surface reconstruction (yellow) following Shimizu et al. (2021) are also indicated for comparison.

The fault we use here has a narrow width, so quasi-two-dimensional interpolation from Shimizu et al. (2021) provides a good approximation if no noise exists. Even for such high-aspect-ratio source faults, nonetheless, the results of this study indicate that a probabilistic approach is beneficial for surface reconstruction from noisy  $n$ -vector fields. Rather than reducing noise through the law of large numbers associated with averaging along the short sides, denoising based on the a priori knowledge that  $n$ -vector components that do not satisfy the slope integrability condition (eq. 11) are fictitious is likely to better reproduce the original shape.

## 6 APPLICATION

Finally, we apply our normal-to-elevation projection to the PDTI involving surface reconstruction (Shimizu et al. 2021). The aim of this section is three-dimensional earthquake fault inference.

### 6.1 Incorporating three-dimensional surface reconstruction with Bayesian PDTI

For the application, we combine the prior constraint on fault geometry  $P(\Gamma|\mathbf{a})$  with the posterior probability of the potency density in the orthodox PDTI. We have considered static problems so far, and hereafter we also consider dynamic problems to invert teleseismic data. The result obtained thus far is applicable as is even when the representation theorem becomes time-dependent and the basis functions are spanned spatiotemporally.

The formulation of the orthodox PDTI, both for static and dynamic problems, consists of the potency likelihood  $P(\mathbf{d}|\mathbf{a}, \Gamma; \sigma^2)$ , which is given by data  $\mathbf{d}$  through the representation theorem, and the prior  $P(\mathbf{a}; \rho^2)$  for the potency density subject to the basis function expansions  $\mathbf{a}$ . The scales of variances for the likelihood  $\sigma^2$  and weight factors for prior loss functions  $\rho^2$  are simultaneously estimated. Usually,  $\sigma^2$  represents the scales of observation errors and Green's function errors (Yagi & Fukahata 2011), and  $\rho^2$  represents the smoothing intensities with respect to space and time (Shimizu et al. 2020). The problem to be solved here consists of these  $P(\mathbf{d}|\mathbf{a}, \Gamma; \sigma^2)$  and  $P(\mathbf{a}; \rho^2)$  and the prior for the surface  $P(\Gamma|\mathbf{a})$ , and its formal solution is the joint posterior of  $\mathbf{a}$  and  $\Gamma$ :

$$P(\mathbf{a}, \Gamma|\mathbf{d}; \sigma^2, \rho^2) = P(\mathbf{d}|\mathbf{a}, \Gamma; \sigma^2)P(\mathbf{a}; \rho^2)P(\Gamma|\mathbf{a})/P(\mathbf{d}; \sigma^2, \rho^2), \quad (39)$$

where

$$P(\mathbf{d}; \sigma^2, \rho^2) = \int d\mathbf{a} d\Gamma P(\mathbf{d}|\mathbf{a}, \Gamma; \sigma^2)P(\mathbf{a}; \rho^2)P(\Gamma|\mathbf{a}). \quad (40)$$

The analysis for the dislocation limit is simplified when the joint posterior  $P(\mathbf{a}, \Gamma|\mathbf{d}; \sigma^2, \rho^2)$  is decomposed into the marginal posterior of the potency  $P(\mathbf{a}|\mathbf{d}; \sigma^2, \rho^2) = \int d\Gamma P(\mathbf{a}, \Gamma|\mathbf{d}; \sigma^2, \rho^2)$  and the conditional posterior of the surface  $P(\Gamma|\mathbf{a}, \mathbf{d}; \sigma^2, \rho^2)$ :

$$P(\mathbf{a}, \Gamma|\mathbf{d}; \sigma^2, \rho^2) = P(\mathbf{a}|\mathbf{d}; \sigma^2, \rho^2)P(\Gamma|\mathbf{a}, \mathbf{d}; \sigma^2, \rho^2). \quad (41)$$

From eq. (16),

$$P(\mathbf{a}|\mathbf{d}; \sigma^2, \rho^2) = P(\mathbf{a}, \Gamma_*(\mathbf{a})|\mathbf{d}; \sigma^2, \rho^2) \quad (42)$$

$$P(\Gamma|\mathbf{a}, \mathbf{d}; \sigma^2, \rho^2) = \delta(\Gamma - \Gamma_*(\mathbf{a})). \quad (43)$$

That is, the evaluation of  $P(\mathbf{a}, \Gamma|\mathbf{d}; \sigma^2, \rho^2)$  is reduced to the alternate recursion of the most probable estimation of  $\Gamma$  given  $\mathbf{a}$  returning  $\Gamma_*$  (eq. 43) and the inference of  $\mathbf{a}$  given  $\Gamma_*$  (eq. 42).



We evaluate the hyperparameter optimals  $\hat{\sigma}^2$  and  $\hat{\rho}^2$  by Akaike's Bayesian Information Criterion (ABIC; Akaike 1980):

$$(\hat{\sigma}^2, \hat{\rho}^2) = \operatorname{argmax}_{\sigma^2, \rho^2} P(\mathbf{d}; \sigma^2, \rho^2). \quad (44)$$

The associated optimals of the potency density and fault surface are evaluated by the posterior maximum:

$$(\hat{\mathbf{a}}, \hat{\Gamma}) = \operatorname{argmax}_{\mathbf{a}, \Gamma} P(\mathbf{a}, \Gamma | \mathbf{d}; \hat{\sigma}^2, \hat{\rho}^2). \quad (45)$$

Neglecting the third- and higher-order moments from the probability peaks as in Shimizu et al. (2021), eqs. (40) and (42) are simplified as

$$P(\mathbf{d}; \sigma^2, \rho^2) \simeq \int d\mathbf{a} P(\mathbf{d} | \mathbf{a}, \hat{\Gamma}; \sigma^2) P(\mathbf{a}; \rho^2) \quad (46)$$

and

$$P(\mathbf{a} | \mathbf{d}; \sigma^2, \rho^2) \simeq \frac{P(\mathbf{d} | \mathbf{a}, \hat{\Gamma}; \sigma^2) P(\mathbf{a}; \rho^2)}{P(\mathbf{d}; \sigma^2, \rho^2)}. \quad (47)$$

Besides, from eqs. (41) and (43),

$$\hat{\Gamma} = \Gamma_*(\hat{\mathbf{a}}). \quad (48)$$

Thus, our optimum-value estimation is the alternate recursion of solving for  $\hat{\Gamma}$  given  $\hat{\mathbf{a}}$  and solving for  $(\hat{\mathbf{a}}, \hat{\sigma}^2, \hat{\rho}^2)$  given  $\hat{\Gamma}$ . The analysis with a fixed  $\Gamma$  is exactly the orthodox source inversion with fixed geometry (Yagi & Fukahata 2011; Shimizu et al. 2020), and the analysis of  $\Gamma$  given  $\mathbf{a}$  is what this study has examined. Once  $\hat{\Gamma}$  and  $(\hat{\sigma}^2, \hat{\rho}^2)$  are obtained, the uncertainty of  $\mathbf{a}$  is evaluable through eq. (47) by using  $P(\mathbf{a} | \mathbf{d}; \hat{\sigma}^2, \hat{\rho}^2)$ . Hyperparameter uncertainty is similarly evaluable using  $P(\mathbf{d}; \sigma^2, \rho^2)$  for given  $\hat{\Gamma}$ , though it is a sharply peaked well-behaved distribution and follows the law of large numbers exceptionally rapidly when  $\sigma^2$  and  $\rho^2$  are exponential loss weights (Sato et al. 2022).

The above procedure does not include explicit  $\Gamma$  uncertainty evaluations. In the present problem setting using a delta-functional  $P(\Gamma | \mathbf{a})$ , the estimation error of  $\Gamma$  solely derives from error propagation from the potency density estimation, and its evaluation requires another joint posterior decomposition  $P(\mathbf{a}, \Gamma | \mathbf{d}; \sigma^2, \rho^2) = P(\Gamma | \mathbf{d}; \sigma^2, \rho^2) P(\mathbf{a} | \Gamma, \mathbf{d}; \sigma^2, \rho^2)$  and the evaluation of  $P(\Gamma | \mathbf{d}; \sigma^2, \rho^2) = \int d\mathbf{a} P(\mathbf{a}, \Gamma | \mathbf{d}; \sigma^2, \rho^2)$ . Due to the slope integrability (eq. 11) on a smooth surface, the posterior of the fault surface  $P(\Gamma | \mathbf{d}; \sigma^2, \rho^2)$  is deviated from the posterior of the  $n$ -vector  $n_*$  field expected from the potency density (Appendix A). The evaluation of  $P(\mathbf{a} | \Gamma, \mathbf{d}; \sigma^2, \rho^2)$  corresponds to the conventional slip inversion, where the potency density  $\mathbf{a}$  is forced to be a displacement discontinuity field across given  $\Gamma$ .

## 6.2 Recipe

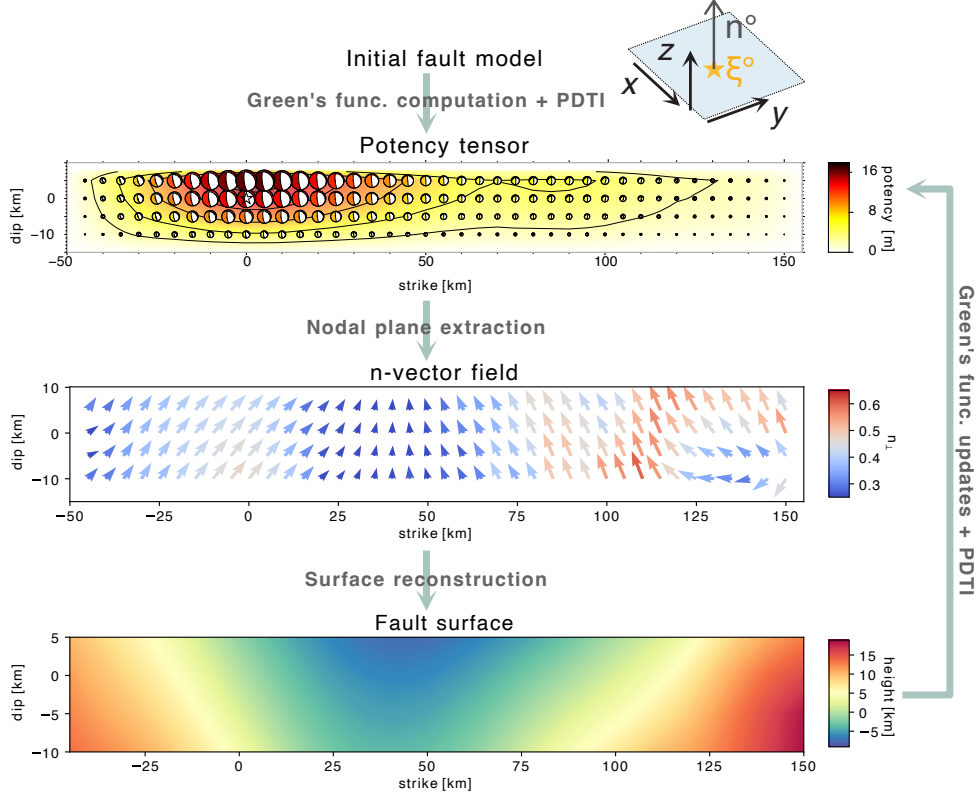
The computations of  $\hat{\mathbf{a}}$ ,  $\hat{\Gamma}$ , and  $(\hat{\boldsymbol{\sigma}}^2, \hat{\boldsymbol{\rho}}^2)$  (eqs. 44 and 45) as per eqs. (46)–(48) are formally the same as those of Shimizu et al. (2021) that alternately evaluate  $(\mathbf{a}, \boldsymbol{\sigma}^2, \boldsymbol{\rho}^2)$  for given  $\Gamma$  and  $\Gamma$  for given  $\mathbf{a}$ . Therefore, simply updating their fault reconstruction stage enables their routine to reconstruct three-dimensional fault geometry.

Figure 9 outlines our computational routine following Shimizu et al. (2021). (I: Fault model initialization) A structured grid is set along the reference plane, and the spatial knots for potency density interpolations are placed at grid centers; non-planar initializations following stage V below are optionally applied. (II: PDTI with Green’s function computations) The PDTI is performed, with Green’s function approximated by point-source representations; when the point sources are allocated to grid centers, they are weighted by the areas of gridded subsurfaces. (III: Nodal plane extraction) The  $n$ -vector estimates of point sources are computed as nodal planes of estimated potency beachballs; the  $n$ -vector field estimate is approximately computed by their interpolation. (IV: Surface reconstruction) The elevation field is reconstructed from the  $n$ -vector field estimate. (V: PDTI with Green’s function updates) The aforementioned structured grid is vertically projected onto the reconstructed fault surface, and the vertical positions of sources and the areas of gridded subsurfaces are updated accordingly; the PDTI updates the potency beachballs and the loop returns to the stage III.

In summary, once the PDTI is performed, potency beachballs set an  $n$ -vector field, which in turn reconstructs the fault surface, the continuous information of which is subdivided as a digital elevation model to update Green’s function for the next PDTI. The digital elevation model is now computed by the Visualization Toolkit (Schroeder et al. 1998), and we call it by using a Python helper PyVista (Sullivan & Kaszynski 2019). We execute the following two operations via PyVista: (A) the projection of the structured grid generated by `numpy.meshgrid` onto the reconstructed fault surface (`pyvista.StructuredGrid`) and (B) the computation of source locations and subdivided areas on vertically projected structured grids (`compute_cell_sizes`, `cell_centers`).

We solve this recursion by a gradient descent, where the  $\Gamma_*$  determination (eq. 35) is modified by a penalty term on the residual elevation from a given shape  $\bar{\Gamma}$  with elevation  $\bar{z}$  as

$$\begin{aligned} \Gamma'_*(\mathbf{a}, \bar{\Gamma}; \lambda) = \operatorname{argmin} \bigg\{ & \int n_{*z} (n_{*||x} n_{*z} z_{,x} + n_{*||y} n_{*z} z_{,y} + n_{*\perp})^2 dx dy \\ & + \int n_{*z} (n_{*||x} z_{,y} - n_{*||y} z_{,x})^2 dx dy + \lambda^{-1} \int |z - \bar{z}|^2 dx dy \bigg\}, \end{aligned} \quad (49)$$



**Figure 9.** A schematic diagram of simultaneous potency and fault shape estimation as per eq. (50). The loop starts with initializing the fault model. The potency tensors obtained by the PDTI are converted to the  $n$ -vector field, which reconstructs the fault surface. The reconstructed surface updates Green’s functions, and alternate potency density and shape inferences restart. The distributed potency beachballs in the figure represent the estimate of the first iteration obtained by Shimizu et al. (2020), and the others refer to the results of Fig. 10.

and each surface update accounts for the pre-update state:

$$\begin{aligned}
 (\hat{\sigma}^{2(n)}, \hat{\rho}^{2(n)}) &:= \operatorname{argmax}_{(\sigma^2, \rho^2)} \int d\mathbf{a} P(\mathbf{d}|\mathbf{a}, \hat{\Gamma}^{(n)}; \sigma^2) P(\mathbf{a}; \rho^2) \\
 \hat{\mathbf{a}}^{(n)} &:= \operatorname{argmax}_{\mathbf{a}} P(\mathbf{d}|\mathbf{a}, \hat{\Gamma}^{(n)}; \hat{\sigma}^{2(n)}) P(\mathbf{a}; \hat{\rho}^{2(n)}) \\
 \hat{\Gamma}^{(n+1)} &:= \Gamma'_*(\hat{\mathbf{a}}^{(n)}, \hat{\Gamma}^{(n)}; \lambda).
 \end{aligned} \tag{50}$$

The elevation  $\hat{z}^{(n)}$  of the  $n$ -th iteration  $\hat{\Gamma}^{(n)}$  is updated to  $\hat{z}^{(n+1)} = \hat{z}^{(n)} + \lambda \partial[\kappa^{-1} \ln P(\Gamma|\hat{\mathbf{a}}^{(n)})]/\partial z$ , and  $\lambda$  is the learning rate of this gradient descent. When iterations converge,  $\hat{z}^{(n)} = \hat{z}^{(n+1)}$  is met, and the surface optimal  $\hat{\Gamma} = \hat{\Gamma}^{(n+1)}$  is the solution that satisfies  $\partial \ln P(\Gamma|\hat{\mathbf{a}})/\partial z = 0$  for  $\hat{\mathbf{a}} = \hat{\mathbf{a}}^{(n)}$ .

### 6.3 Case study of the 2013 Balochistan earthquake

The 2013 Balochistan earthquake struck southwestern Pakistan on 24 September 2013. It is moment magnitude (Mw) 7.7 oblique strike-slip faulting, yet variations in the centroid moment tensor solutions

and geological features (e.g. Avouac et al. 2014; Jolivet et al. 2014) may collectively suggest source complexities typified by fault nonplanarity. Its slip zone is the Hoshab fault situated in the transition between the Chaman fault system and the accretionary wedge (Avouac et al. 2014), so a wedge-slicing listric fault is likely; however, it was hard for multiple point source approaches to constrain whether the listric or non-listric fault is the preferred geometry for this earthquake (Jolivet et al. 2014). The PDTI detects major along-strike variations of potency tensors as well as minor along-dip variations, but three-dimensional geometry construction was beyond the reach of previous efforts (Shimizu et al. 2020, 2021). Enabling the PDTI to reconstruct three-dimensional geometry, we attempt to extract the listric geometry of this earthquake fault.

Data and data processing in this application follow those of Shimizu et al. (2020), which consist of observed vertical components of teleseismic P waveforms converted to velocities at 36 stations shown in Figs. 2(c) and S1 of Shimizu et al. (2021). The only update from the method and data of Shimizu et al. (2021) is the three-dimensional fault reconstruction of eq. (50).

Previous studies have shown that the solution updates could mostly finish with the first iteration (Shimizu et al. 2021), so it would be helpful to delve into the initial surface reconstruction. Figure 10 plots the surface reconstruction from the potency beachballs distributed over the reference plane (Shimizu et al. 2020), which is the same initial input as that of Shimizu et al. (2021). The reference plane is taken as a vertical plane through the hypocenter with a strike angle of 226 degrees, setting the southwest and the upward positive. Figure 10 employs  $\lambda^{-1} = 0$  and uses eq. (35) as in the synthetic tests. Normal vectors evaluated from the PDTI provide expected fault slopes as an input set (Fig. 10a). The fault elevation field is then reconstructed as an output (Fig. 10b). Slopes of the reconstructed surface well explain the input slopes (Fig. 11). Residuals of  $n$ -vectors are generally random, with some correlation with neighboring points due to smoothing imposed on the potency density estimate. The smooth surface reconstruction provides subfault elevations and subfault areas for horizontal fault subdivision, which convert the areal density of potency to distributed potency sources, updating Green's function for the PDTI of the next iteration.

Iterative shape updates are shown in Fig. 12. The shape is quickly constrained at the center of large slips, and the convergence is slow at the edges of small slips, where the constraint is relatively weak. High learning rates vibrate poorly constrained regions (fault edges in Fig. 12a–d) while low learning rates slow down updates (Fig. 12i–l), as is often the case with gradient descents. The inference with adjusted learning rates converges to the optimal within a few iterations (Fig. 12e–h). The first surface reconstruction of relatively high learning rates (Fig. 12b) outlines a converged fault shape, as in a quasi-two-dimensional approach by Shimizu et al. (2021). Our estimate progressively approaches the surface rupture identified in the field survey (Zinke et al. 2014, Fig. 12 red line) in spite of not

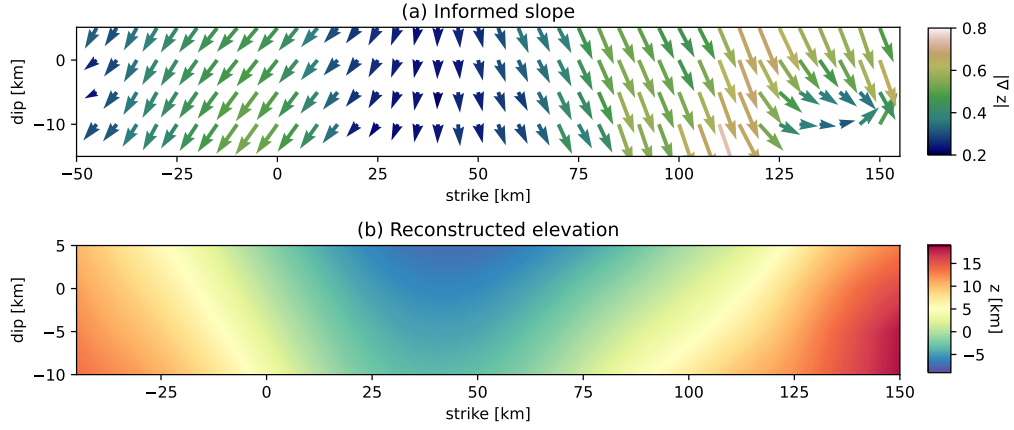


**Figure 10.** Surface reconstruction from the potency distributed over a reference plane. (a) Informed fault slopes, calculated from the estimated  $n$ -vector field via eq. (7). Collocation points of informed slopes correspond to the  $x$ - $y$  locations of B-spline knots for potency densities. (b) Reconstructed fault elevation when using eq. (35).

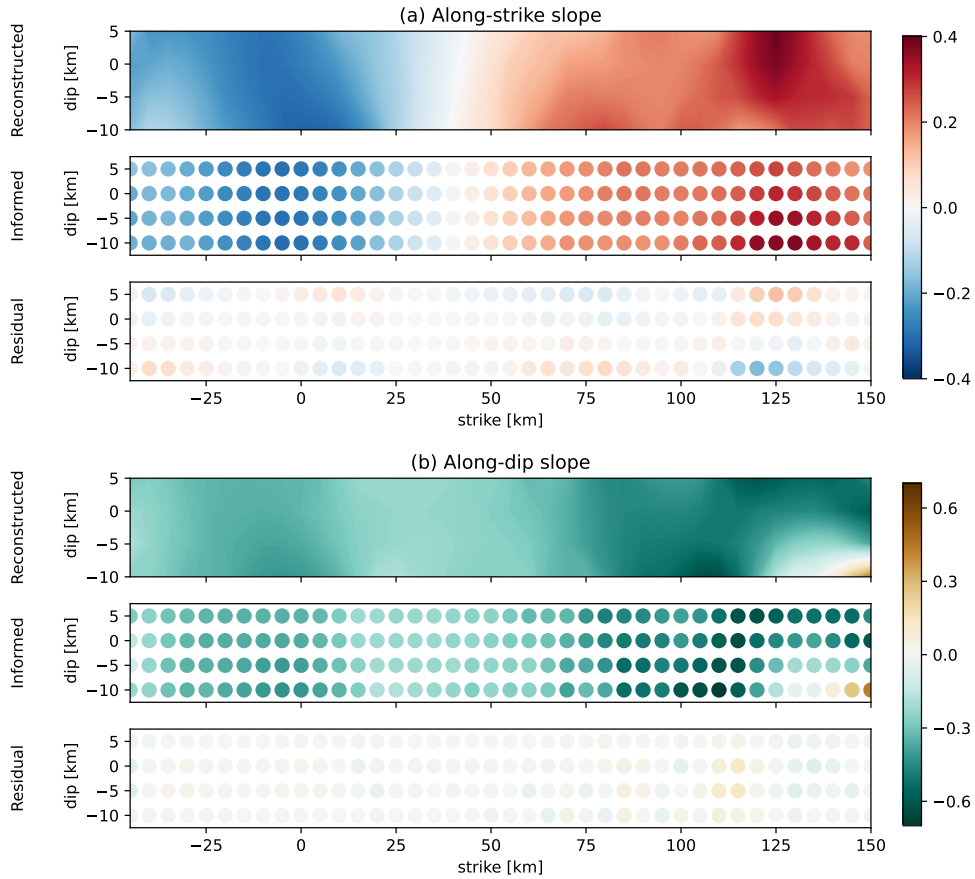


**Figure 11.** Comparisons between reconstructed and informed slopes along strike (a) and dip (b). Reconstructed and informed slopes correspond to Fig. 10b and Fig. 10a, respectively. Their residuals are also indicated.

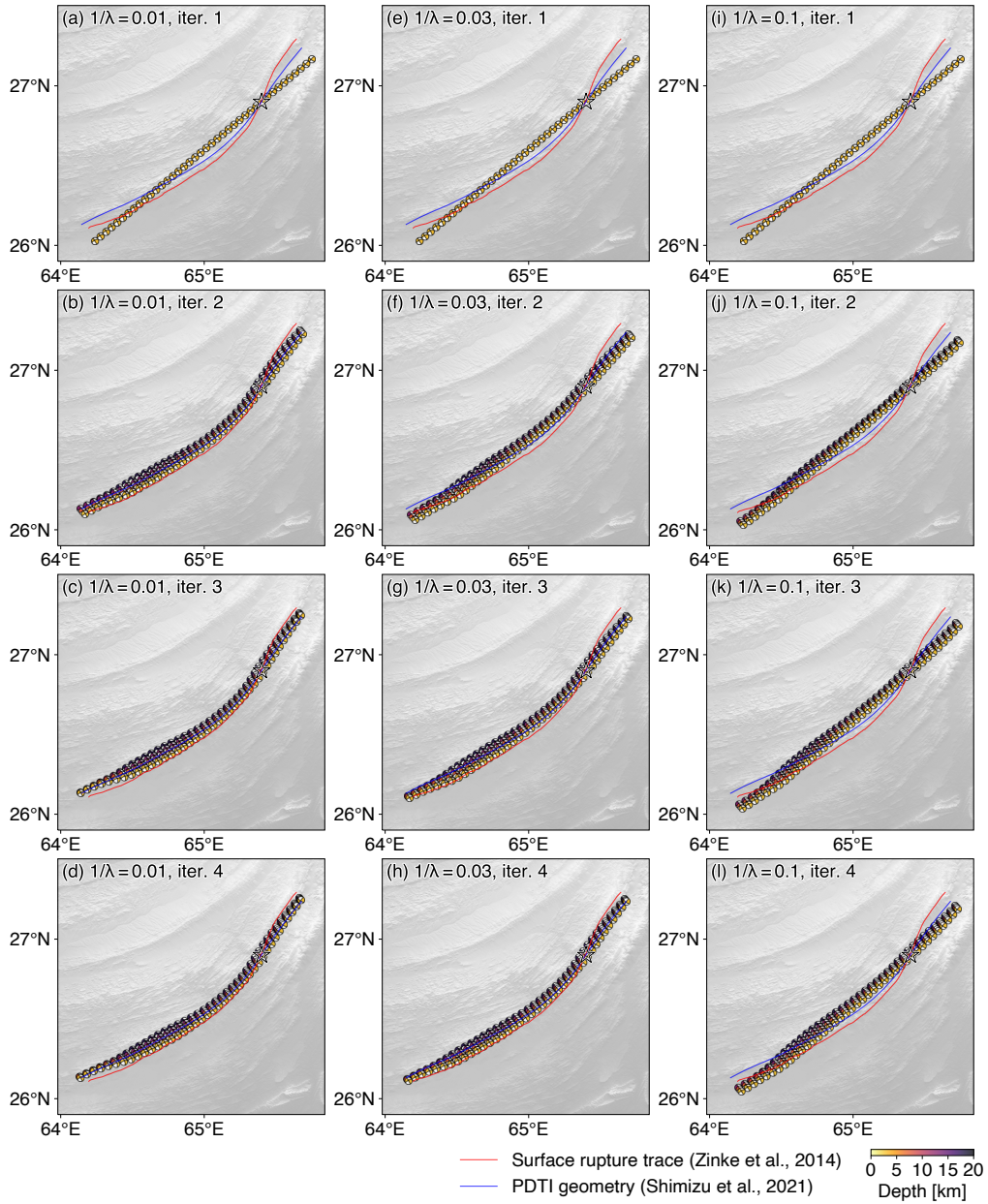


**Figure 12.** Iterations of computed gradient descents. The first to fourth iterations are shown for the learning rate inverse  $\lambda^{-1}$  of 0.01 (a–d), 0.03 (e–h), and 0.1 (i–l). The star shows the epicenter, and the background topography is from SRTMGL1 (NASA JPL 2013). The surface rupture trace (Zinke et al. 2014, red) and two-dimensional geometry reconstructed in the previous PDTI (Shimizu et al. 2021, blue) are drawn for comparison.

incorporating the surface trace. In Shimizu et al. (2021), the dip was fixed at 90 degrees so that their estimate (Fig. 12, blue line) shifted northward from the surface trace near 50 km southwest of the hypocenter, and it is resolved in the present inversion.

We thus obtain the optimal solution as in Fig. 13 ( $\lambda^{-1} = 0.03$ , sixth iteration). The along-strike curve is steeper at shallower depths, and the dip angle becomes sharper at greater depths, so the

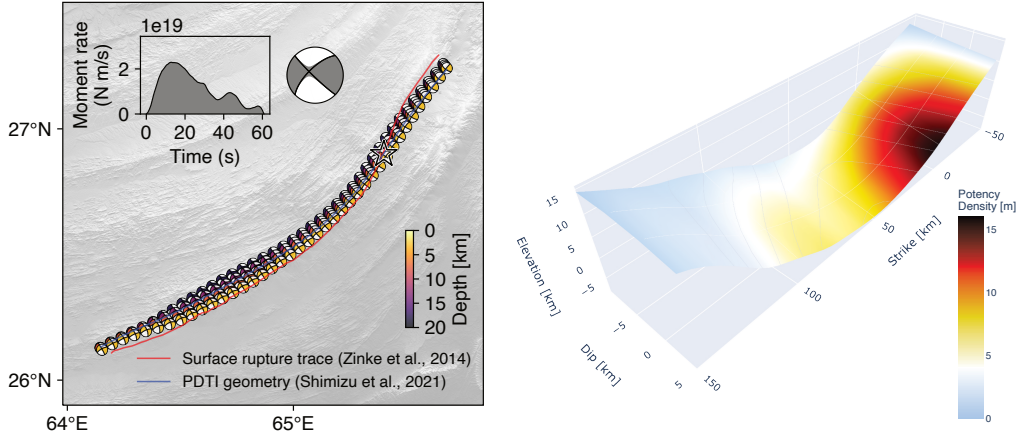


**Figure 13.** Our optimal source model ( $\lambda^{-1} = 0.03$ , the sixth iteration). Distributed potency tensors are shown in the birds-eye view with the epicenter indicated by the star (left), and the absolute potency densities are projected onto the reconstructed fault surface (right). The fault surface elevation is evaluated against a reference vertical plane with a 226-degree strike angle, the origin of which is the hypocenter. The moment rate function and the moment beachball obtained by the space-time integral of the potency-rate density tensors are also plotted.

reconstructed fault forms a bowl-shaped surface. It agrees with the geometry expected for a listric fault. Although the input  $n$ -vectors corresponding to the B-spline knots of the PDTI have only four points along the dip, the reconstructed surface draws along-strike-varying along-dip variations. Such smooth strike-and-dip variations had already been captured by the beachball nodal planes without performing surface reconstruction (Fig. 11), but the three-dimensional surface reconstruction has made the interpretation more intuitive. Along-depth elevations of a few dozen kilometers are consistent with the constant-dip fault model of Jolivet et al. (2014) that is generated from distributed point source modeling. At the same time, like the other model of Jolivet et al. (2014) oriented to the geological setting of listric faults, the fault reconstructed in this study holds three-dimensional attributes.

Since the dip angle unnaturally flips near 150 km strike at depth (Fig. 9), the accuracy around the southwestern edge is doubtful. The non-slipping zone is suggested to be poorly constrained even with prior information on the smoothness of potency densities. It may be overcome by trimming source faults, for example, by using informatics to determine the minimum number of beachballs required to describe source faults (Thurin 2024), and the same might apply to the decision of the number of faults. The elevation north of the epicenter is estimated systematically lower than the surface trace as in Shimizu et al. (2021), and it is likely due to smoothing out a near-hypocenter stepover visible in the surface trace. The use of surface rupture traces as an a priori constraint would bring fault shapes closer to the actual. The method validation is in progress as above, but anticipating that case studies ensue

and reveal the workings of the fault reconstruction from potency, we submit the result of the simplest method (eq. 50) as a baseline solution.

## 7 CONCLUDING REMARKS

We study surface reconstruction from the potency field, where a smooth surface is constructed from the estimated  $n$ -vector field pointed by the nodal planes of estimated potency beachballs. The contribution of this work is the derivation of a formula that enables the three-dimensional surface reconstruction left behind by Shimizu et al. (2021). Our investigation reveals that the three-dimensional surface reconstruction is overdetermined, thus necessitating a stochastic approach. This transition is inevitable in the surface reconstruction from potency. The same could apply to surface reconstruction from distributed point sources, and our formulation is applicable to surface reconstruction from multiple coseismic focal mechanisms (Yue & Lay 2020), aftershock hypocenters (Fuenzalida et al. 2013; Wang et al. 2021; Sawaki et al. 2025), and earthquake swarms (Yukutake et al. 2011; Ross et al. 2020). Given the above nature of surface reconstruction elucidated, we have formulated and solved the problem of stochastic surface reconstruction from a given  $n$ -vector field, and our synthetic tests confirm that the solution of this problem reproduces the original surface from noisy  $n$ -vector data. Even for narrow faults, three-dimensional probabilistic approaches can better reproduce the original shape than deterministic quasi-two-dimensional approaches. A preliminary analysis of the 2013 Balochistan earthquake captured along-dip shape variability that was not reconstructed by Shimizu et al. (2021). There remains a jump to actual applications, but at present, it works.

## ACKNOWLEDGMENTS

The first author D.S. acknowledges valuable comments from Dr. Haruo Horikawa. This work was in part supported by JSPS KAKENHI Grant Numbers JP21H05206 and JP25K01084.

## Data availability

Waveform data inverted in our application are downloaded from the Seismological Facility for the Advancement of Geoscience Data Management Center and processed in Shimizu et al. (2020). The ground topography in this paper refers to SRTMGL1 (NASA JPL 2013).



## REFERENCES

- Akaike, H., 1980. Likelihood and the Bayes procedure, in “Bayesian Statistics”, ed. by jm bernardo, mh degroot, dv lindley, and afm smith.
- Aki, K., 1979. Characterization of barriers on an earthquake fault, *Journal of Geophysical Research: Solid Earth*, **84**(B11), 6140–6148.
- Ando, R. & Kaneko, Y., 2018. Dynamic rupture simulation reproduces spontaneous multifault rupture and arrest during the 2016 Mw 7.9 Kaikoura earthquake, *Geophysical Research Letters*, **45**(23), 12–875.
- Aspri, A., Beretta, E., Mazzucato, A. L., & De Hoop, M. V., 2020. Analysis of a model of elastic dislocations in geophysics, *Archive for Rational Mechanics and Analysis*, **236**, 71–111.
- Aspri, A., Beretta, E., Lee, A., & Mazzucato, A. L., 2025. A shape derivative algorithm for reconstructing elastic dislocations in geophysics, *Research in the Mathematical Sciences*, **12**(2), 24.
- Avouac, J.-P., Ayoub, F., Wei, S., Ampuero, J.-P., Meng, L., Leprince, S., Jolivet, R., Duputel, Z., & Helmburger, D., 2014. The 2013, Mw 7.7 Balochistan earthquake, energetic strike-slip reactivation of a thrust fault, *Earth and Planetary Science Letters*, **391**, 128–134.
- Barka, A. & Kadinsky-Cade, K., 1988. Strike-slip fault geometry in Turkey and its influence on earthquake activity, *Tectonics*, **7**(3), 663–684.
- Beretta, E., Francini, E., & Vessella, S., 2008. Determination of a linear crack in an elastic body from boundary measurements—lipschitz stability, *SIAM journal on mathematical analysis*, **40**(3), 984–1002.
- Bruhat, L., Fang, Z., & Dunham, E. M., 2016. Rupture complexity and the supershear transition on rough faults, *Journal of Geophysical Research: Solid Earth*, **121**(1), 210–224.
- Das, S. & Aki, K., 1977. Fault plane with barriers: A versatile earthquake model, *Journal of geophysical research*, **82**(36), 5658–5670.
- Diao, H., Liu, H., & Meng, Q., 2023. Dislocations with corners in an elastic body with applications to fault detection, *arXiv preprint arXiv:2309.09706*.
- Dutta, R., Jónsson, S., & Vasyura-Bathke, H., 2021. Simultaneous Bayesian estimation of non-planar fault geometry and spatially-variable slip, *Journal of Geophysical Research: Solid Earth*, **126**(7), e2020JB020441.
- Fan, W., Okuwaki, R., Barbour, A. J., Huang, Y., Lin, G., & Cochran, E. S., 2022. Fast rupture of the 2009 Mw 6.9 Canal de Ballenas earthquake in the Gulf of California dynamically triggers seismicity in California, *Geophysical Journal International*, **230**(1), 528–541.
- Fuenzalida, A., Schurr, B., Lancieri, M., Sobiesiak, M., & Madariaga, R., 2013. High-resolution relocation and mechanism of aftershocks of the 2007 tocopilla (chile) earthquake, *Geophysical Journal International*, **194**(2), 1216–1228.
- Fukahata, Y. & Wright, T. J., 2008. A non-linear geodetic data inversion using abic for slip distribution on a fault with an unknown dip angle, *Geophysical Journal International*, **173**(2), 353–364.
- Howarth, J. D., Barth, N. C., Fitzsimons, S. J., Richards-Dinger, K., Clark, K. J., Biasi, G. P., Cochran, U. A., Langridge, R. M., Berryman, K. R., & Sutherland, R., 2021. Spatiotemporal clustering of great earthquakes on a transform fault controlled by geometry, *Nature Geoscience*, **14**(5), 314–320.

- Inoue, N., Yamaguchi, R., Yagi, Y., Okuwaki, R., Bogdan, E., & Tadapansawut, T., 2025. A multiple asymmetric bilateral rupture sequence derived from the peculiar tele-seismic P-waves of the 2025 Mandalay, Myanmar earthquake, *Seismica*, **4**(1), doi: 10.26443/seismica.v4i1.1691.
- Jolivet, R., Duputel, Z., Riel, B., Simons, M., Rivera, L., Minson, S., Zhang, H., Aivazis, M., Ayoub, F., Leprince, S., et al., 2014. The 2013 Mw 7.7 Balochistan earthquake: seismic potential of an accretionary wedge, *Bulletin of the Seismological Society of America*, **104**(2), 1020–1030.
- Kasahara, A. & Yagi, Y., 2010. Complex seismic source inversion method with the data covariance matrix: Application to the 2010 Haiti earthquake, in *AGU Fall Meeting Abstracts*, vol. 2010, pp. S43A–2024.
- Kase, Y. & Day, S., 2006. Spontaneous rupture processes on a bending fault, *Geophysical Research Letters*, **33**(10).
- Kikuchi, M. & Kanamori, H., 1991. Inversion of complex body waves—III, *Bulletin of the Seismological Society of America*, **81**(6), 2335–2350.
- Kodaira, S., Hori, T., Ito, A., Miura, S., Fujie, G., Park, J.-O., Baba, T., Sakaguchi, H., & Kaneda, Y., 2006. A cause of rupture segmentation and synchronization in the Nankai trough revealed by seismic imaging and numerical simulation, *Journal of Geophysical Research: Solid Earth*, **111**(B9).
- Loveless, J. P. & Meade, B. J., 2010. Geodetic imaging of plate motions, slip rates, and partitioning of deformation in Japan, *Journal of Geophysical Research: Solid Earth*, **115**(B2).
- Mallick, R. & Meade, B. J., 2025. Smooth slip is all you need: A singularity-free boundary element method for fault slip problems, *Computers & Geosciences*, **196**, 105820.
- Matsu'ura, M., 1977a. Inversion of geodetic data Part I. mathematical formulation, *Journal of Physics of the Earth*, **25**(1), 69–90.
- Matsu'ura, M., 1977b. Inversion of geodetic data. Part II. Optimal model of conjugate fault system for the 1927 Tango earthquake, *Journal of Physics of the Earth*, **25**(3), 233–255.
- Matsu'ura, M. & Hasegawa, Y., 1987. A maximum likelihood approach to nonlinear inversion under constraints, *Physics of the Earth and planetary interiors*, **47**, 179–187.
- Matsu'ura, M., Noda, A., & Terakawa, T., 2019. Physical interpretation of moment tensor and the energetics of shear faulting, *Tectonophysics*, **771**, 228228.
- NASA JPL, 2013. NASA Shuttle Radar Topography Mission Global 1 arc second [Data set], *NASA EOSDIS Land Processes Distributed Active Archive Center*, doi: 10.5067/MEaSUREs/SRTM/SRTMGL1.003.
- Ohara, K., Yagi, Y., Yamashita, S., Okuwaki, R., Hirano, S., & Fukahata, Y., 2023. Complex evolution of the 2016 Kaikoura earthquake revealed by teleseismic body waves, *Progress in Earth and Planetary Science*, **10**(1), 35.
- Okuwaki, R., Hirano, S., Yagi, Y., & Shimizu, K., 2020. Inchworm-like source evolution through a geometrically complex fault fueled persistent supershear rupture during the 2018 Palu Indonesia earthquake, *Earth and Planetary Science Letters*, **547**, 116449.
- Ozawa, S., Ando, R., & Dunham, E. M., 2023. Quantifying the probability of rupture arrest at restraining and releasing bends using earthquake sequence simulations, *Earth and Planetary Science Letters*, **617**, 118276.

- Ragon, T., Sladen, A., & Simons, M., 2018. Accounting for uncertain fault geometry in earthquake source inversions—i: theory and simplified application, *Geophysical Journal International*, **214**(2), 1174–1190.
- Romanet, P., Sato, D. S., & Ando, R., 2020. Curvature, a mechanical link between the geometrical complexities of a fault: Application to bends, kinks and rough faults, *Geophysical Journal International*, **223**(1), 211–232.
- Romanet, P., Saito, T., & Fukuyama, E., 2024. The mechanics of static non-planar faults in infinitesimal strain theory, *Geophysical Journal International*, **239**(3), 1664–1693.
- Ross, Z. E., Cochran, E. S., Trugman, D. T., & Smith, J. D., 2020. 3d fault architecture controls the dynamism of earthquake swarms, *Science*, **368**(6497), 1357–1361.
- Sato, D. S., Fukahata, Y., & Nozue, Y., 2022. Appropriate reduction of the posterior distribution in fully Bayesian inversions, *Geophysical Journal International*, **231**(2), 950–981.
- Sawaki, Y., Shiina, T., Sagae, K., Sato, Y., Horikawa, H., Miyakawa, A., Imanishi, K., & Uchide, T., 2025. Fault geometries of the 2024 mw 7.5 noto peninsula earthquake from hypocenter-based hierarchical clustering of point-cloud normal vectors, *Journal of Geophysical Research: Solid Earth*, **130**(4), e2024JB030233.
- Schroeder, W., Martin, K. M., & Lorensen, W. E., 1998. *The visualization toolkit an object-oriented approach to 3D graphics*, Prentice-Hall, Inc.
- Shimizu, K., Yagi, Y., Okuwaki, R., & Fukahata, Y., 2020. Development of an inversion method to extract information on fault geometry from teleseismic data, *Geophysical Journal International*, **220**(2), 1055–1065.
- Shimizu, K., Yagi, Y., Okuwaki, R., & Fukahata, Y., 2021. Construction of fault geometry by finite-fault inversion of teleseismic data, *Geophysical Journal International*, **224**(2), 1003–1014.
- Sullivan, C. & Kaszynski, A., 2019. Pyvista: 3D plotting and mesh analysis through a streamlined interface for the Visualization Toolkit (VTK), *Journal of Open Source Software*, **4**(37), 1450.
- Tadapansawut, T., Okuwaki, R., Yagi, Y., & Yamashita, S., 2021. Rupture process of the 2020 Caribbean earthquake along the Oriente transform fault, involving supershear rupture and geometric complexity of fault, *Geophysical Research Letters*, **48**(1), e2020GL090899.
- Thurin, J., 2024. Sparse fault representation based on moment tensor interpolation, *Seismica*, **3**(2).
- Tsai, V. C., Nettles, M., Ekström, G., & Dziewonski, A. M., 2005. Multiple cmt source analysis of the 2004 sumatra earthquake, *Geophysical Research Letters*, **32**(17).
- Volkov, D., Voisin, C., & Ionescu, I. R., 2017. Reconstruction of faults in elastic half space from surface measurements, *Inverse Problems*, **33**(5), 055018.
- Wang, W., Fang, L., Wu, J., Tu, H., Chen, L., Lai, G., & Zhang, L., 2021. Aftershock sequence relocation of the 2021 ms 7.4 maduo earthquake, qinghai, china, *Science China Earth Sciences*, **64**, 1371–1380.
- Wei, G., Chen, K., & Meng, H., 2023. Bayesian inversion of finite-fault earthquake slip model using geodetic data, solving for non-planar fault geometry, variable slip, and data weighting, *Journal of Geophysical Research: Solid Earth*, **128**(2), e2022JB025225.
- Yabuki, T. & Matsu'ura, M., 1992. Geodetic data inversion using a Bayesian information criterion for spatial distribution of fault slip, *Geophysical Journal International*, **109**(2), 363–375.
- Yagi, Y. & Fukahata, Y., 2010. Waveform inversion for seismic source processes with uncertainty of Green's

function, in *AGU Fall Meeting Abstracts*, vol. 2010, pp. S53C–1990.

Yagi, Y. & Fukahata, Y., 2011. Introduction of uncertainty of Green’s function into waveform inversion for seismic source processes, *Geophysical Journal International*, **186**(2), 711–720.

Yagi, Y., Okuwaki, R., Hirano, S., Enescu, B., Chikamori, M., & Yamaguchi, R., 2024. Barrier-induced rupture front disturbances during the 2023 Morocco earthquake, *Seismological Research Letters*, **95**(3), 1591–1598.

Yue, H. & Lay, T., 2020. Resolving complicated faulting process using multi-point-source representation: Iterative inversion algorithm improvement and application to recent complex earthquakes, *Journal of Geophysical Research: Solid Earth*, **125**(2), e2019JB018601.

Yukutake, Y., Ito, H., Honda, R., Harada, M., Tanada, T., & Yoshida, A., 2011. Fluid-induced swarm earthquake sequence revealed by precisely determined hypocenters and focal mechanisms in the 2009 activity at hakone volcano, japan, *Journal of Geophysical Research: Solid Earth*, **116**(B4).

Zinke, R., Hollingsworth, J., & Dolan, J. F., 2014. Surface slip and off-fault deformation patterns in the 2013 Mw 7.7 Balochistan, Pakistan earthquake: Implications for controls on the distribution of near-surface coseismic slip, *Geochemistry, Geophysics, Geosystems*, **15**(12), 5034–5050.

## APPENDIX A: ESTIMATION ERROR PROPAGATION FROM POTENCY TO FAULT SHAPE

The prior of shape  $P(\Gamma|\mathbf{a})$  shown in §3 and the posterior of potency  $P(\mathbf{a}|\mathbf{d})$  [ $P(\mathbf{a}|\mathbf{d}; \sigma^2, \rho^2)$  in the text] set the marginal posterior of fault shape:

$$P(\Gamma|\mathbf{d}) = \int d\mathbf{a} P(\Gamma|\mathbf{a}) P(\mathbf{a}|\mathbf{d}). \quad (\text{A.1})$$

Here we show the procedure to translate  $P(\mathbf{a}|\mathbf{d})$  into  $P(\Gamma|\mathbf{d})$  when  $P(\Gamma|\mathbf{a})$  satisfies  $n \xrightarrow{\mathcal{P}} n_*$  (eq. 13).

For brevity, we introduce the (marginal) posterior of the  $n$ -vector field  $\{\mathbf{n}_*\}$  associated with the potency density:

$$P(\{\mathbf{n}_*\}|\mathbf{d}) = \int d\mathbf{a} P(\mathbf{a}|\mathbf{d}) \int d\xi \delta(\mathbf{n}_*(\xi) - \mathbf{n}_*(\xi; \mathbf{a})). \quad (\text{A.2})$$

$P(\{\mathbf{n}_*\}|\mathbf{d})$  and  $P(\Gamma|\mathbf{a})$  of eq. (14) rewrite the marginal posterior of the fault shape as

$$P(\Gamma|\mathbf{d}) = \int d\{\mathbf{n}_*\} P(\{\mathbf{n}_*\}|\mathbf{d}) \exp[\kappa \int d\xi \mathbf{n} \cdot \mathbf{n}_*] / \mathcal{Z}, \quad (\text{A.3})$$

the right-hand side of which describes the transformation from the posterior  $P(\{\mathbf{n}_*\}|\mathbf{d})$  of the fault normal  $\{\mathbf{n}_*\}$  anticipated from potency into the posterior  $P(\Gamma|\mathbf{d})$  of fault shape. Especially when  $\kappa \rightarrow \infty$ ,  $\exp[\kappa \int d\xi \mathbf{n} \cdot \mathbf{n}_*]$  is extremely sharper than  $P(\{\mathbf{n}_*\}|\mathbf{d})$  and satisfies  $n \xrightarrow{\mathcal{P}} n_*$  (eq. 13), leading to

$$P(\Gamma|\mathbf{d}) = c \int d\{\mathbf{n}_*\} P(\{\mathbf{n}_*\}|\mathbf{d}) \int d\xi \delta(\mathbf{n}(\xi) - \mathbf{n}_*(\xi)), \quad (\text{A.4})$$

where  $c$  denotes normalization. Contrary to its appearance, eq. (A.4) does not conclude that the poste-

rior  $P(\Gamma|\mathbf{d})$  of fault surface  $\Gamma$  equals the posterior  $P(\{\mathbf{n}_*\}|\mathbf{d})$  of the potency-conforming  $n$ -vector  $\mathbf{n}_*$ :  $P(\Gamma|\mathbf{d}) \neq P(\{\mathbf{n}_*\}|\mathbf{d})|_{\mathbf{n}_*=\mathbf{n}}$ . The  $\mathbf{n}_*$ -vector field determined from potency can exceed the definition domain of the  $n$ -vector field on a smooth surface  $\Gamma$  bounded by the surface slope integrability (eq. 11) as indicated in §3, and therefore eq. (A.4) becomes

$$P(\Gamma|\mathbf{d}) = cP(\{\mathbf{n}_*\}|\mathbf{d})|_{\mathbf{n}_*=\mathbf{n} \cap \partial_x(n_y/n_z)=\partial_y(n_x/n_z)}. \quad (\text{A.5})$$

Thus, searching for the optimum  $n$ -vector field of a smooth surface from the posterior of potency is a conditional optimization constrained by  $\partial_x(n_y/n_z) = \partial_y(n_x/n_z)$ . The inference of the optimum elevation automatically satisfies  $\partial_x(n_y/n_z) = \partial_y(n_x/n_z)$  and evades this complication as in §3. The surface reconstruction from this  $P(\Gamma|\mathbf{d})$  is generally a non-linear analysis based on eq. (37) relating surface normal  $\mathbf{n}$  and surface slope  $\nabla z$ . The evaluation of eq. (37) passes through the similar procedure to that shown in §4.2. Equation (A.5) also applies to  $P(\Gamma|\mathbf{a})$  other than eq. (14) when  $n \xrightarrow{\mathcal{P}} n_*$  (eq. 13) is met.

We must remark that the non-uniqueness of functional forms of  $P(\Gamma|\mathbf{a})$ , which was an issue in surface reconstruction from given potency, does not matter in surface reconstruction from the posterior probability of potency  $P(\Gamma|\mathbf{d})$  (eq. A.5). It could answer why the overdetermination of surface reconstruction from potency has not posed an issue in slip inversions on a movable fault surface. After all, we must embrace either the subjectivity inherent in projecting observed inelastic strains onto displacement discontinuities or the subjectivity that forbids all but displacement discontinuities:  $P(\mathbf{a}, \Gamma|\mathbf{d}) = P(\mathbf{a}|\mathbf{d})P(\Gamma|\mathbf{a}, \mathbf{d}) \rightarrow P(\mathbf{a}|\mathbf{d})P(\Gamma|\mathbf{a})$  in the text or  $P(\mathbf{a}, \Gamma|\mathbf{d}) = P(\mathbf{a}|\Gamma, \mathbf{d})P(\Gamma|\mathbf{d})$  equivalent to the slip inversions with a movable fault surface (§6.1).

## APPENDIX B: THE EXACT SOLUTION OF $\Gamma_*$ FOR FINITE $(\partial_x\partial_y - \partial_y\partial_x)z_*$

The evaluation of  $\Gamma_*$  in the text (§4.2) has assumed that the non-integrable component  $(\partial_x\partial_y - \partial_y\partial_x)z_*$  expected from the  $n$ -vector  $\mathbf{n}_*$  of potency is small. Its motive is to avoid an issue of  $P(\Gamma|\mathbf{a})$  selection arising from finite  $(\partial_x\partial_y - \partial_y\partial_x)z_*$  (§3, the last paragraph). For deeper considerations, we show below the way to evaluate  $\Gamma_*$  for given  $P(\Gamma|\mathbf{a})$  for finite  $(\partial_x\partial_y - \partial_y\partial_x)z_*$ . We treat eq. (14) with  $\kappa \rightarrow \infty$  as a concrete example, and similar results follow other forms of  $P(\Gamma|\mathbf{a})$ .

Even in the dislocation limit  $n \xrightarrow{\mathcal{P}} n_*$  (eq. 13,  $\kappa \rightarrow \infty$  for eq. 14), the  $n$ -vector of a surface is necessarily deviated from the expectation  $\mathbf{n}_*$  of potency due to the non-integrable components of  $(\partial_x\partial_y - \partial_y\partial_x)z_*$ . What is expected in this limit is the smallness of the fluctuations from  $\mathbf{n}_*$  with non-integrable components removed, that is, the  $n$ -vector of  $\Gamma_*$  to be sought itself. This  $n$ -vector of  $\Gamma_*$ , the

solution to be sought, is here denoted by  $\mathbf{n}'_*$ :

$$\lim_{\kappa \rightarrow \infty} \mathbf{n}(\boldsymbol{\xi}) = \mathbf{n}'_*(\boldsymbol{\xi}; \Gamma). \quad (\text{B.1})$$

Therefore, if  $(\partial_x \partial_y - \partial_y \partial_x) z_*$  is finite, the fast convergent series in the dislocation limit is the Taylor series of  $\mathbf{n}$  around  $\mathbf{n}'_*$ , not the Taylor series of  $\mathbf{n}$  around  $\mathbf{n}_*$  conducted in the text.

We now perform this corrected series expansion to account for  $(\partial_x \partial_y - \partial_y \partial_x) z_*$  components dropped in §4.2. By utilizing

$$\begin{pmatrix} \frac{\partial}{\partial \theta} \\ \frac{\partial}{\partial \phi} \end{pmatrix} (\mathbf{n} \mathbf{e}_\theta \mathbf{e}_\phi) = \begin{pmatrix} \mathbf{e}_\theta & -\mathbf{n} & \mathbf{0} \\ \mathbf{e}_\phi \sin \theta & \mathbf{e}_\phi \cos \theta & -\mathbf{n} \sin \theta - \mathbf{e}_\theta \cos \theta \end{pmatrix}, \quad (\text{B.2})$$

we obtain the second-order representation of  $\mathbf{n}$  around  $\mathbf{n}'_*$  with respect to the angle fluctuations  $\delta\Omega'$  from  $\mathbf{n}'_*$ :

$$\begin{aligned} \mathbf{n} = & \left[ 1 - \frac{1}{2}(\theta - \theta'_*)^2 - \frac{\sin^2 \theta'_*}{2}(\phi - \phi'_*)^2 \right] \mathbf{n}'_* \\ & + \left[ (\theta - \theta'_*) - \frac{1}{2} \sin \theta'_* \cos \theta'_* (\phi - \phi'_*)^2 \right] \mathbf{e}_\theta^{*'} \\ & + [\sin \theta'_* (\phi - \phi'_*) + \cos \theta'_* (\theta - \theta'_*) (\phi - \phi'_*)] \mathbf{e}_\phi^{*'}, \end{aligned} \quad (\text{B.3})$$

where  $(\theta'_*, \phi'_*)$  denotes the position of  $\mathbf{n}'_*$  on a unit sphere, and  $\mathbf{e}_\theta^{*'}$  and  $\mathbf{e}_\phi^{*'}$  represent associated basis vectors; higher orders become infinitesimally smaller in the dislocation limit. Especially for  $P(\Gamma|\mathbf{a})$  of eq. (14) with  $\kappa \rightarrow \infty$ ,

$$\mathbf{n}_* \cdot \mathbf{n} = \mathbf{n}'_* \cdot \mathbf{n} - (\mathbf{n}'_* - \mathbf{n}_*) \cdot \mathbf{n} \quad (\text{B.4})$$

$$= \left[ 1 - \frac{1}{2}(\theta - \theta'_*)^2 - \frac{\sin^2 \theta'_*}{2}(\phi - \phi'_*)^2 \right] - (\mathbf{n}'_* - \mathbf{n}_*) \cdot \mathbf{n}. \quad (\text{B.5})$$

The first term replicates the right-hand side of eq. (26) with  $(\theta_*, \phi_*)$  substituted with  $(\theta'_*, \phi'_*)$  and thus functions similarly to those seen in the text. The second term is the correction arising from the deviation of  $\mathbf{n}'_*$  from  $\mathbf{n}_*$ , explicitly written as

$$\begin{aligned} (\mathbf{n}'_* - \mathbf{n}_*) \cdot \mathbf{n} = & \left[ 1 - \frac{1}{2}(\theta - \theta'_*)^2 - \frac{\sin^2 \theta'_*}{2}(\phi - \phi'_*)^2 \right] (1 - \mathbf{n}_* \cdot \mathbf{n}'_*) \\ & - \left[ (\theta - \theta'_*) - \frac{1}{2} \sin \theta'_* \cos \theta'_* (\phi - \phi'_*)^2 \right] (\mathbf{n}_* \cdot \mathbf{e}_\theta^{*'}) \\ & - [\sin \theta'_* (\phi - \phi'_*) + \cos \theta'_* (\theta - \theta'_*) (\phi - \phi'_*)] (\mathbf{n}_* \cdot \mathbf{e}_\phi^{*'}). \end{aligned} \quad (\text{B.6})$$

Angle fluctuations  $\theta - \theta'_*$  and  $\phi - \phi'_*$  are expressed by eqs. (31) and (32) in the text with a substitution  $(\theta_*, \phi_*) \rightarrow (\theta'_*, \phi'_*)$ :

$$\theta - \theta'_* = -n_{*z}'^2 (n_{*||x}' z_{,x} + n_{*||y}' z_{,y} + n_{*||z}' / n_{*z}') \quad (\text{B.7})$$

$$\phi - \phi'_* = -n_{*\perp}'^{-1} n_{*z}' (n_{*||x}' z_{,y} - n_{*||y}' z_{,x}). \quad (\text{B.8})$$

The rest is unaltered from the text, and the final result is:

$$\begin{aligned} \Gamma_* = \operatorname{argmin} \int d\Sigma \{ & [(\theta - \theta'_*)^2 + \sin^2 \theta'_* (\phi - \phi'_*)^2] (\mathbf{n}_* \cdot \mathbf{n}'_*) \\ & + [-2(\theta - \theta'_*) + \sin \theta'_* \cos \theta'_* (\phi - \phi'_*)^2] (\mathbf{n}_* \cdot \mathbf{e}_{\theta}^{*'}) \\ & - 2[\sin \theta'_* (\phi - \phi'_*) + \cos \theta'_* (\theta - \theta'_*) (\phi - \phi'_*)] (\mathbf{n}_* \cdot \mathbf{e}_{\phi}^{*'}) \}. \end{aligned} \quad (\text{B.9})$$

Equation (B.9) is a self-consistent equation, where the condition to determine  $\Gamma_*$  contains the  $n$ -vector of  $\Gamma_*$  ( $\mathbf{n}'_*$ ) and the basis vectors ( $\mathbf{e}_{\theta}^{*'}$  and  $\mathbf{e}_{\phi}^{*'}$ ) at the spherical position  $(\theta'_*, \phi'_*)$  of that  $n$ -vector. For small  $(\partial_x \partial_y - \partial_y \partial_x) z_*$ ,  $\mathbf{n}'_* \simeq \mathbf{n}_*$  holds, and the correction becomes negligible, resulting in eq. (35) of the main text. Although the above correction is not accounted for in the main text supposing small  $(\partial_x \partial_y - \partial_y \partial_x) z_*$ , the correction may be iteratively computed with the initialization of  $\mathbf{n}'_* \simeq \mathbf{n}_*$ . The correction for  $P(\Gamma|\mathbf{a})$  other than eq. (14) is similarly evaluated using eqs. (B.3), (B.7), and (B.8).